

國立交通大學
光電工程研究所
碩士論文

非極性氮化銦薄膜之兆赫波輻射研究

Terahertz Emission Properties of
Nonpolar Indium Nitride Film

研究生：何介曄

指導教授：潘犀靈 教授

安惠榮 教授

中華民國九十七年七月

非極性氮化銦薄膜之兆赫波輻射研究

Terahertz Emission Properties of
Nonpolar Indium Nitride Film

研 究 生：何介暉

Student : Chieh-Wei He

指 導 教 授：潘犀靈 教授

Advisors : Prof. Ci-Ling Pan

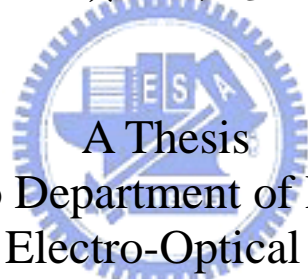
安惠榮 教授

Prof. Hyeyoung Ahn

國立交通大學

光電工程研究所

碩士論文



A Thesis

Submitted to Department of Photonics and
Institute of Electro-Optical Engineering
College of Electrical Engineering
National Chiao Tung University
In partial Fulfillment of the Requirements
for the Degree of
Master of Science
in

Electro-Optical Engineering

July 2008

Hsinchu, Taiwan, Republic of China

中華民國九十七年七月

國立交通大學

論文口試委員會審定書

本校光電工程研究所碩士班何介曄君

所提論文非極性氮化銅薄膜之兆赫波輻射研究

合於碩士資格標準、業經本委員會評審認可。

口試委員：趙如蘋
(趙如蘋 教授)

李晁達
(李晁達 教授)

陳瓊華
(陳瓊華 教授)

指導教授：馮厚靈 安惠榮

所長：趙子強 教授

系主任：黃中堯 教授

中華民國 97 年 7 月 30 日

非極性氮化銦薄膜之兆赫波輻射研究

學生：何介暉

指導教授：潘犀靈教授

安惠榮教授

國立交通大學光電工程研究所

摘要

在這篇論文中，我們研究有關 c 軸平面氮化銦薄膜與 a 軸平面氮化銦薄膜之光激發產生兆赫波輻射研究。我們的團隊曾報導過源自於奈米柱狀結構的兆赫波輻射強度增強現象，相較於 c 軸平面氮化銦薄膜所產生者在兆赫波輻射電場上大上十倍，並且我們認為這兩種結構的氮化銦薄膜都是以 photo-Dember effect 作為輻射兆赫波的主要機制。對於沿著 a 軸 $\langle 11\bar{2}0 \rangle$ 成長的平面而言，極化導致的電場平行於表面介面，我們並且發現其兆赫波放射能量上遠遠比 c 軸平面氮化銦薄膜大上兩個級數，且與目前所知最好的兆赫波放射源：砷化銦擁有相同級數的輻射強度。我們認為 a 軸平面氮化銦薄膜主要的兆赫波輻射機制是來自於受激發載子在極化感應電場下有著較為有效率輻射出半導體介面的幾何耦合輻射效應。

在高能量雷射的激發之下，放射出的兆赫波顯示出與方位角有關的分量疊加於與方位角無關的分量上。與激發光線的線性偏振和方位角有關的兆赫波輻射特性可能是來自於兆赫波的非線性輻射，例如光整流效應，此與 a 軸平面氮化銦薄膜的電納系數有著密切關係。

Terahertz Emission Properties of Nonpolar Indium Nitride Film

Student : Chieh-Wei He

Advisors : Prof. Ci-Ling Pan

Prof. Hyeyoung Ahn

Department of Photonics and Institute of Electro-Optic Engineering, College of Electrical Engineering
National Chiao Tung University

Abstract

In this thesis, we report the terahertz emission measurement from c -plane and a -plane indium nitride (InN) films. Our group already has reported the enhancement of terahertz (THz) radiation (greater than ten times in intensity) from InN nanorod arrays compared to the InN films grown along the c -axis and the dominant emission mechanism was proposed to be the photo-Dember effect. For the layers grown along a - $\langle 11\bar{2}0 \rangle$, polarization-induced electric field is parallel to the layer interface and THz emission from it is found to be at least two orders of magnitude stronger than that from c -plane InN film, which is the same order of InAs, the best semiconductor THz emitter so far. We propose that the primary radiation mechanism of the a -plane InN film is due to the acceleration of photoexcited carriers under the polarization-induced in-plane electric field perpendicular to the a -axis, which effectively enhances the geometrical coupling of the radiation out of semiconductor.

At high photoexcitation, emitted THz wave shows the obvious azimuthal angle dependence superimposed with a strong angle-independent component. Pump polarization and azimuthal angle dependence of emitted THz wave may be due to the nonlinear THz emission mechanism, such as optical rectification, which is depending on the characteristic susceptibility tensor of a -plane InN.

Acknowledgement

這本論文能夠完成首先要感謝我的指導老師潘犀靈教授與安惠榮教授無私的指導，他們教導我擁有正確的實驗方法與態度，經由討論分析實驗數據釐清許多實驗上的疑難雜症，使我從大學時代僅埋首書本而無實作經驗的學生轉變成能夠對於一套實驗系統鉅細靡遺描述與闡論的研究生。此外，也要感謝清大果尚志老師實驗室提供實驗所需的樣品，並在製程與量測上給予我很大的幫助。

另外，還要感謝王怡超學長在雷射系統的架設與維護上竭盡所能的指導與幫忙，並教導我許多雷射系統上的知識，讓我能夠在專心實驗之餘沒有後顧之憂。

再者，還要感謝和我一起努力的實驗室伙伴，除了在研究領域上的討論與辨析讓我對實驗理論有更深層的認知外，平時生活相處的點滴更讓人銘記心頭。

最後，感謝我的家人從小到大對我的栽培，即便在這兩年的研究生涯中共同經歷了許多人生無法避免的無常與創傷，他們仍舊給予我一美好的家庭環境與親情，於我情緒低落時提供最強大的精神後盾，在生活無虞的前提下讓我能專心致志於攻讀碩士學位。還有，我最親愛的爺爺奶奶，您們永遠是我在人生道路上的楷模。雖然這本論文不是什麼驚天動地的非凡研究，然而記錄刻印這兩年間的實驗歷程與成果，希望它能夠讓您們引以為傲。

平安有愛

Peace

Contents

Abstract(C)	i
Abstract(E)	ii
Acknowledgement	iii
Contents	iv
List of Figures	vi
List of Tables	x
Chapter 1 Introduction	1
1-1 Terahertz Radiation.....	1
1-2 III-Nitride Compound Semiconductors : InN.....	5
1-3 Organization of Thesis.....	7
Chapter 2 Experimental Theories	8
2-1 Terahertz Generation.....	8
2-1-1 Surge-Current Model.....	8
2-1-2 Surface Depletion Field.....	10
2-1-3 Photo-Dember Effect.....	12
2-1-4 Optical Rectification.....	16
2-1-5 THz Enhancement by External Magnetic Field	19
2-2 Terahertz Detection : Electro-Optical Crystal and Free Space	

Electro-Optic Sampling (FS-EOS)	21
Chapter 3 Experimental Setups	25
3-1 Introduction of Femtosecond Laser System	25
3-2 Electro-Optic THz System.....	27
Chapter 4 Sample Properties.....	31
4-1 InN Film (c-plane InN).....	33
4-2 Nonpolar InN Film (a-plane InN).....	34
Chapter 5 Experimental Results and Discussion.....	37
5-1 Terahertz Emission from InN Surface	37
5-2 Azimuthal Angle dependence of InN.....	45
5-3 Pump Polarization Dependence of Semiconductors.....	51
Chapter 6 Conclusion and Future Work	55
6-1 Conclusion	55
6-2 Future Work	56

List of Figures

Fig 1-1 The spectrum range of electromagnetic waves.....	1
Fig 1-2 The energy band gaps of Group-III nitride semiconductors. The ternary system InGaN can match the solar spectral irradiance as shown at the right side.....	6
Fig 2-1. Band diagram and the schematic flow of drift current in a typical n-type semiconductor.....	12
Fig 2-2 Schematic flow of diffusion current by photo-excited carriers.....	15
Fig 2-3 Optical geometry of THz radiation from a semiconductor surface.....	18
Fig 2-4 Azimuthal angle dependence of THz radiation amplitude from semi-conductors with (a) n-InAs (111) and (b) n-InSb.....	18
Fig 2-5. Schematic diagram of the experimental geometry and coordinate system....	21
Fig 2-6 Schematic figure of Electro-optic sampling.....	24
Fig 3-1. Femtosecond laser system includes Tsunami, Spitfire and two pump laser (Millennia V and Empower).....	26
Fig 3-2. Electro-Optic THz system.....	29
Fig 3-3. THz time-domain (a) waveform and (b) its corresponding spectrum generated by the electro-optic THz system using a-plane InN as emitter under the humidity of 55%	30

Fig 3-4. THz time-domain (a) waveform and (b) its corresponding spectrum generated by the electro-optic THz system using a-plane InN as emitter under the humidity of 5%30

Fig 4-1 Simplified view of the band edge structure of InN.32

Fig 4-2. Crystal structure of InN.....33

Fig 4-3 The SEM pictures of c-plane InN film. [This picture is taken from the Prof. S. Gwo’s group, The Department of Physics, National Tsing Hua University.]34

Fig 4-4. RT Hall mobility and carrier concentration of *a*-plane InN films as a function of film thickness. The inset shows the corresponding data of the *c*-plane InN films.35

Fig 4-5. The SEM pictures of a-plane InN film. [This picture is taken from the Prof. S. Gwo’s group, The Department of Physics, National Tsing Hua University.]36

Fig 5-1 The amplitude of the terahertz emission from a-plane InN film (red solid line) compare to that from c-plane InN film. The excitation is 0.24 mJ/cm². Inset: comparison between a-plane InN , c-plane InN measure under identical experimental condition.....40

Fig 5-2 Schematic diagram of the experimental geometry and coordinate system.[30]

.....42

Fig 5-3 Calculated polar radiation patterns for GaAs at (a) 0 and (b) 8 T. In each part the horizontal line is a schematic representation of the surface of the semiconductor. The bow-tie pattern below the surface line is calculated for radiation within the semiconductor, whereas the pattern above the surface shows the radiation emitted into free-space. The vector **B** indicates the magnetic-field direction.42

Fig 5-4 Ball-and-stick model of the a-plane surface. Large balls are In, small balls are N.

.....44

Fig 5-5 Optical reflectivities in InN-epilayer and nonpolar InN as a function of excitation energy. Optical absorption in InN film is about 80%, while that in nonpolar InN is about 76%.44

Fig 5-6. Peak amplitude of terahertz emission for c-plane InN film (red points) and a-plane InN film (black points) as a function of laser pump power.....45

Fig 5-7. Azimuthal-angle dependence of THz-emission amplitude from n-InAs.....46

Fig 5-8. Peak amplitude of the p-terahertz fields as function of azimuthal angel rotation of (a) c-plane InN film and (b) a-plane InN excited at 20mW.....49

Fig 5-9. Peak amplitude of the p-terahertz fields as function of azimuthal angel rotation of a-plane InN film excited at different fluence (a) 20mW (b) 50mW (c) 75mW (d) 100 mW by p-polarized pump beam.49

Fig 5-10 The amplitude of the p-polarized THz emission field vs pump fluence at the different azimuthal angle. θ_1 is the angle with minimum azimuthal modulation and θ_2 is the angle with maximum azimuthal modulation50

Fig 5-11. Azimuthal-angle dependence of the a-plane InN film with the pump power 50mW and p-polarized pump beam.50

Fig 5-12. Azimuthal-angle dependence of the a-plane InN film with the pump power 50mW and s-polarized pump beam.50

Fig5-13 Pump polarization angle dependence of THz peak amplitude of c-plane InN. The pump polarization is p-polarization when angles are at 0° , 180° , 360° and s-polarization when angles are at 90° , 270° . The maximum peak is at the p-pump and the minimum peak amplitude at the s-pump.....51

Fig 5-14 .Pump polarization angle dependence of THz peak amplitude of n-type InAs.51

Fig 5-15. Peak amplitude of the p-polarized terahertz fields as function of pump polarization of a-plane InN excited at 20mW. The pump polarization is p-polarization when angles are at 0° , 180° , 360° and s-polarization when angles are at 90° , 270°53

List of Tables

Table 2-1. Band structure parameters of InN and InAs.	15
Table 3-1. Properties of Tsunami laser and Ti:Sapphire regenerative amplifier.	26
Table 4-1. The bandgap energies of some semiconductors.	31
Table 4-2. Properties of the III-Nitride compound semiconductors.	32



Chapter 1 Introduction

1-1 Terahertz Radiation

In the past years, a significant development of ultrafast terahertz (THz) technique has been observed. The application of the THz technique has made significant contribution not only to ultrafast phenomena but also to a wide variety of applications, including ultrahigh speed optoelectronics, tomographic imaging in biomedical fields.

Terahertz (THz) radiation, lies in the frequency gap between the infrared and microwaves(see Fig. 1-1), is typically referred to as the frequencies from 100 GHz to 30 THz which are between microwaves and visible light. 1 THz is equivalent to 33.33 cm^{-1} (wave numbers), 4.1 meV photon energy, or $300 \text{ }\mu\text{m}$ wavelength, so THz waves are also called sub-millimeter wave.

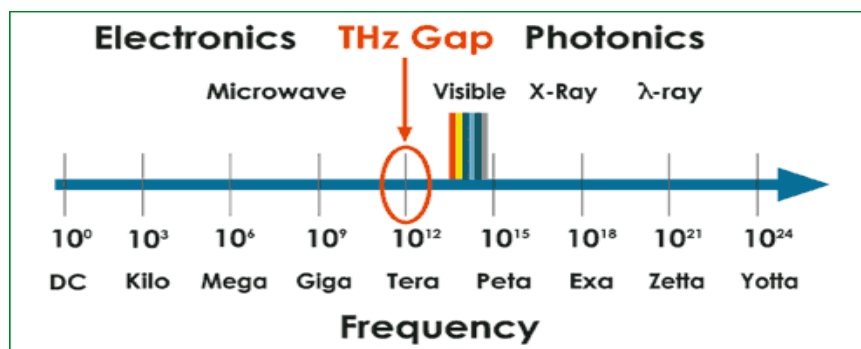


Fig. 1-1 The spectrum range of electromagnetic waves
(http://www.rpi.edu/terahertz/about_us.html)

At lower frequencies compared to THz wave, microwaves can be easily generated by “electronic” devices, such as a simple dipole antenna. At higher frequencies, visible

light can be generated by “optical” devices, such as a semiconductor laser diode, in which electrons jump across the energy band gap and then emit light. Until 1980’s, the spectral range of THz has been inaccessible in both electronic and optical methods. Until then, Fourier transform spectroscopy is perhaps the most common technique to study sub-THz phenomena.

The appearance of ultrashort pulse laser of ~100 fs pulse duration made it possible to generate THz waves covering the whole THz spectral range. In 1981, Mourou and Auston first demonstrated generation and detection of pulsed THz radiation by a photo-conducting switch with advantages of time resolution of picosecond and high sensitivity enhanced by phase-lock technique [1][2]. In 1988, Grischkowsky used the photoconductor dipole antenna as the THz sensor, furthering the spectrum into the order of terahertz frequency [3]. Afterward a variety of antennas was appeared, like typical dipole antenna, large aperture photoconductor dipole antenna [4] and also another method using semiconductor surface electric field [5] to generate THz pulses by the ultrashort pulse laser. In 1996, X. C. Zhang et al. developed free-space electro-optic sampling (FS-EOS) technique to enhance signal to noise ratio (S/N ratio) up to 10^5 and to achieve much large dynamic range [6].

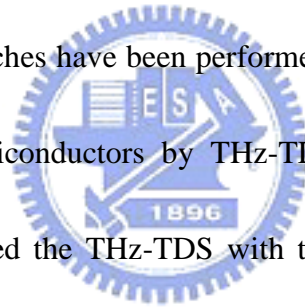
Compared to X-ray, terahertz waves has much smaller photon energy (4.1 meV), therefore, this kind of non-destruction measurement can be used on biology and

medical sciences [7]. Image and tomography [8] of THz have also been studied and can be applied to homeland security.

For semiconductors measurement, conventional four point probe and Hall effect measurement can measure the characteristics including mobility, carrier concentration and resistivity of the semiconductor materials by direct sample contact. All these electrical measurements measure only DC value of the sample but some characteristics like refractive index and conductivity are frequency-dependent. For some semiconductors with high resistivity and low concentration, the electrical properties are difficult to be measured by simple direct contact because the Schottky barrier may disturb the measurement value at the metal-semiconductors interface. Therefore, THz-TDS is desirable for semiconductors characterization due to the advantages of non-contact and frequency-dependant measure. In 1990 D. Grischkowsky *et al.* [9] successfully measured optical properties including refractive index and conductivity of GaAs wafer and the results fit well with the Drude model. Besides GaAs, other semiconductors such as silicon [10] have also been widely studied. Recently, many nanostructured semiconductors like InP-nanoparticle[11], ZnO-nanowire[12], Si-nanoparticle[13] have been studied using THz-TDS technology and the particular conduction behavior have been observed. In comparison with conventional far-IR source and detector, THz-TDS is

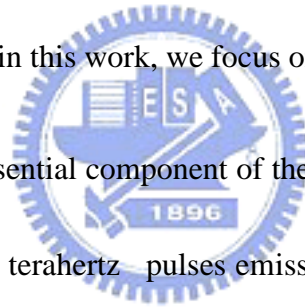
a coherent technology that could obtain both amplitude and phase information simultaneously. Both absorption coefficient and refractive index could be extracted without use of Kramers-Kronig relation, therefore, it simplifies the analysis process.

Recently, the spectroscopic technique using pulsed THz radiation, called "terahertz time-domain spectroscopy (THz-TDS)", has been developed, by taking advantage of short pulses of broadband THz radiation. THz-TDS has the time resolution of sub-picosecond level and the spectral resolution of 50 GHz and THz-TDS is a non-destructive method to the carrier concentration and mobility of doped semiconductors. Many researches have been performed on a variety of gases, liquids, dielectric materials and semiconductors by THz-TDS. For example, in 1990, D. Grischkowsky et al.[9] studied the THz-TDS with the dielectric materials, such as quartz and sapphire, and semiconductors, like silicon and GaAs. They discovered different carrier concentrations affect the absorption characteristics of the samples in the THz frequency range.



1-2 III-Nitride Compound Semiconductors: InN

Group-III nitride semiconductors and their alloys have attracted a lot of attention due to their unique properties for fundamental research and potential applications. Recent research has shown that the bandgap of InN is actually 0.7 eV [13]. Alloyed with GaN, the ternary system InGaN has been shown to cover a wide, continuous spectral range from the near infrared for InN to the near ultraviolet for GaN. Currently there is research into developing solar cells using the nitride based semiconductors. Using the alloy indium gallium nitride, an optical match to the solar spectrum is obtained (see Fig. 1-2). Thus, in this work, we focus on the properties of InN.



Indium nitride, as an essential component of the III-nitride system, has received much attention about ultrafast terahertz pulses emission generated by Indium nitride film layers in recent years. Indium nitride is an interesting and potentially important semiconductor material due to the low bandgap, the high electron mobility. In the other hand, the intervalley scattering is the main reason to increase the effective mass of the photo-generated electrons, and accordingly reduce the Photo-Dember field in the case of InAs. Therefore, the absence of any intervalley scattering is another advantage to use InN as the THz emitter. There have been some several reports on THz emission from InN films [14][15][16]. The THz radiation emitted from InN films is typically one order of magnitude weaker than that from InAs, although the main THz emission

mechanism of both materials is the Photo-Dember effect.

In the past researches, we had shown the enhancement of terahertz radiation (>10 times in intensity) from InN nanorod arrays compared to the InN films grown along the *c*-axis (*c*-plane InN). Because electron accumulation layer at the surface of *c*-plane InN is very thin (< 10nm) and its contribution to terahertz generation is assumed to be negligibly small, the dominant emission mechanism is proposed to be the photo-Dember effect.

In this research, we want to study the whole emission mechanism of the *a*-plane InN film. The *a*-plane InN film grown along the *a*-axis (*a*-plane InN) were rarely reported mainly due to the technical difficulty in growing high crystalline quality *a*-plane InN films and none were reported for their terahertz emission properties. We find that the THz emission from the InN film grown along the *a*-axis (*a*-plane InN) is stronger than that from the InN film grown along the *c*-axis (*c*-plane InN) about one order and suppose this enhancement due to the terahertz dipole formed in the favorable in-plane direction for *a*-plane InN. In the other hand, the azimuthal angle dependence and pump polarization dependence of *a*-plane InN is also different to the *c*-plane one. These results may demonstrate there are quite different mechanism for THz emission between *a*-plane InN and *c*-plane InN.

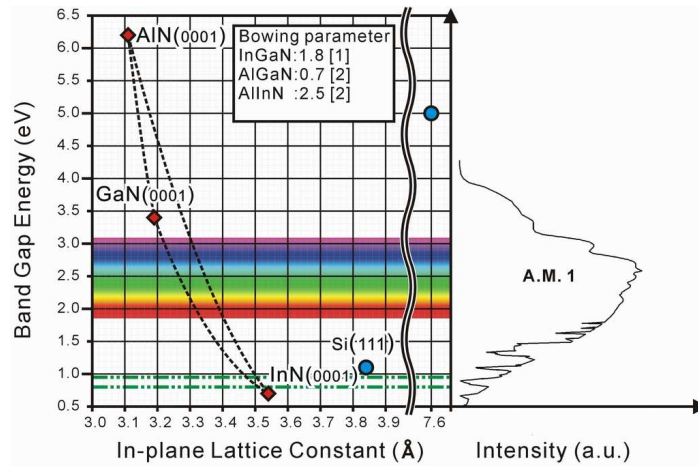


Fig. 1-2 The energy band gaps of Group-III nitride semiconductors. The ternary system InGaN can match the solar spectral irradiance as shown at the right side.

1-3 Organization of Thesis

In chapter 1, an overview of THz radiation and the III-Nitride compound semiconductors: InN are presented. In chapter 2, the experimental theories including THz radiation and detection are interpreted. In chapter 3, the basic characteristics including growth method and Hall measurement results of the semiconductor samples studied in this thesis are described. In chapter 4, the experimental setups including the laser system and the THz-TDS systems are introduced. The experimental results and discussion will be presented in chapter 5. Finally, our conclusions and future work are shown in chapter 6.

Chapter 2 Experimental Theories

2-1 Terahertz Generation

The THz pulse has been generated by different methods, such as irradiation of photo-conductive antenna, semiconductor surfaces, or quantum structures with femtosecond optical pulses. The most common emission mechanisms are surge current and transient polarization which acts as broadband terahertz sources. As the sample is illuminated by an ultrashort laser pulse, electron-hole pairs are created in semiconductors, and then the carriers are accelerated by the external or internal electrical field to form a transient current which radiate THz waves. In this work, the THz waves are generated via surge-current model, which will be described in detail in the next section.

2-1-1 Surge-Current Model

From Maxwell's equation, we have two inhomogeneous wave equations in terms of electric potential V and magnetic potential \vec{A} [17]:

$$\nabla^2 \vec{A} - \epsilon\mu \frac{\partial^2 \vec{A}}{\partial t^2} = -\mu \vec{j} \quad (2-1-1.1)$$

$$\nabla^2 V - \epsilon\mu \frac{\partial^2 V}{\partial t^2} = -\frac{\rho}{\epsilon} \quad (2-1-1.2)$$

where \vec{J} is the current density and ρ is the charge density. These equations describe the propagation of the electromagnetic disturbances. In terms of these potential, the electric field \vec{E} is expressed as

$$\vec{E} = -\nabla V - \frac{\partial \vec{A}}{\partial t} \quad (2-1-1.3)$$

The continuity equation of free carriers which is generated in the emitter after the absorption of an optical pulse is obtained directly from Maxwell's equation:

$$\nabla \cdot (\nabla \cdot \vec{H}) = \nabla \cdot \left(\vec{J} + \frac{\partial \vec{D}}{\partial t} \right) = \nabla \cdot \vec{J} + \frac{\partial \rho}{\partial t} \quad (2-1-1.4)$$

The current is a transverse current which is perpendicular to the direction of propagation, so that we have $\nabla \cdot \vec{J} = 0$. Eq (2-1-1.1) and Eq (2-1-1.4) (all the vector arrows should be corrected) imply that the charge density is constant in time and will not contribute to the time dependent radiated electric field. Therefore, from Eq (2.3) we have

$$\vec{E}_{\text{rad}}(t) = -\frac{\partial}{\partial t} \vec{A}(t) \quad (2-1-1.5)$$

The solution to the wave equation (2-1-1.1) and hence for the vector potential \vec{A} leads to the expression for the time-dependent radiated electric field $\vec{E}_{\text{rad}}(t)$ at a displacement \vec{r} from the center of the emitter:

$$\vec{E}_{\text{rad}}(\vec{r}, t) = -\frac{1}{4\pi\epsilon_0 c^2} \frac{\partial}{\partial t} \int \frac{\vec{J}_s\left(\vec{r}', t - \frac{|\vec{r} - \vec{r}'|}{c}\right)}{|\vec{r} - \vec{r}'|} d\vec{a}' \quad (2-1-1.6)$$

where ϵ_0 is the permittivity of free space, c is speed of light in vacuum, \vec{J}_s is the surface current in emitter evaluated at the retarded time, and $d\vec{a}'$ is the increment of surface area at a displacement \vec{r}' from the center of the emitter. In the far field and assuming \vec{J}_s is a constant at all points in the emitter, the radiated field can be written as

$$\vec{E}_{\text{rad}}(\vec{r}, t) = \frac{b}{r} \frac{d}{dt} \vec{J}_s(t) \quad (2-1-1.7)$$

where b is a constant, and the radiated field is proportional to the time derivative of photo-current.



2-1-2 Surface Depletion Field

In semiconductors with wide bandgap, such as GaAs (1.43 eV) and InP (1.34 eV), there may exist surface states in the forbidden gaps between valance and conduction bands due to the discontinuous structures in the surface. These states with occupied or vacant would affect the equilibrium concentration of electrons and holes in the surface. Because the Fermi-level is position independent, the energy bands must bend to form a depletion region where the surface built-in field exists. The strength of

surface-depletion field is a function of Schottky [18] barrier potential and dopant concentration Eq (2.1.2-1)

$$E_d(x) = \frac{eN}{\epsilon}(W - x) \quad (2-1-2.1)$$

Where N is dopant concentration, ϵ is semiconductor permittivity, and W is depletion width and has the form of Eq (2.1.2-2)

$$W = \sqrt{\frac{2\epsilon}{eN} \left[V - \frac{kT}{e} \right]} \quad (2-1-2.2)$$

Where V is the potential barrier and kT/e is the thermal energy. The direction and magnitude of the surface depletion field depend on the dopant or impurity species and the position of the surface states relative to the bulk Fermi level. In general, the energy band is bent upward and downward for n-type and p-type semiconductors, respectively.

After optical excitation, the electrons and holes are accelerated in opposite directions under the surface-depletion field, forming a surge current in the direction normal to the surface as shown in Fig. 2-1. Therefore, when the depletion surface field is the dominant mechanism for the surge current, the polarity of the emitted THz radiation waveform is opposite between that of the n-type and that of the p-type semiconductor.

Contrarily, if the dominant mechanism is Photo-Dember effect, the emitted THz radiation waveform will be same direction either the n-type semiconductor or the p-type semiconductor, as explained in Section 2.1.3. Thus, by comparing the polarity of

the THz waveforms emitted from an n-type semiconductor and that of the p-type semiconductor, we can determine which mechanism is dominant in the semiconductor.

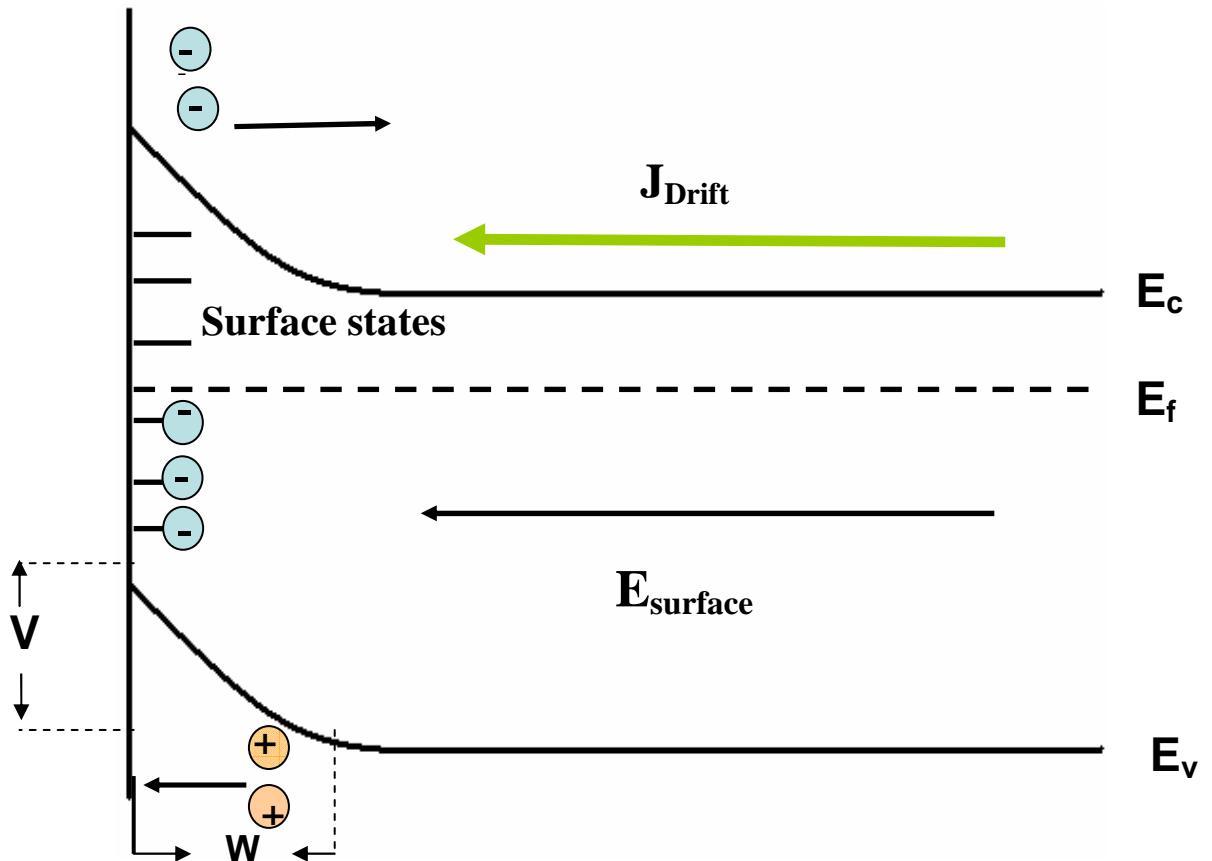


Fig 2-1. Band diagram and the schematic flow of drift current in a typical n-type semiconductor.

2-1-3 Photo-Dember Effect

The role of main band structure parameters such as carrier effective mass and valley energy separations, crucially affect the THz radiation from semiconductor

surfaces. Some semiconductors such as InAs and InN with small band gap and small effective electron mass (Table 2-1) would radiate THz via Photo-Dember effect. With NIR light, the absorption depth is very small($\approx 100\text{nm}$) and the excess energy of photo-excited carriers is very large for the excitation of narrow-bandgap semiconductors. All these conditions in the narrow-bandgap semiconductors enhance the photo-Dember effect, which is known to generate current or voltage in semiconductors due to the difference diffusion velocities of the electron and hole.

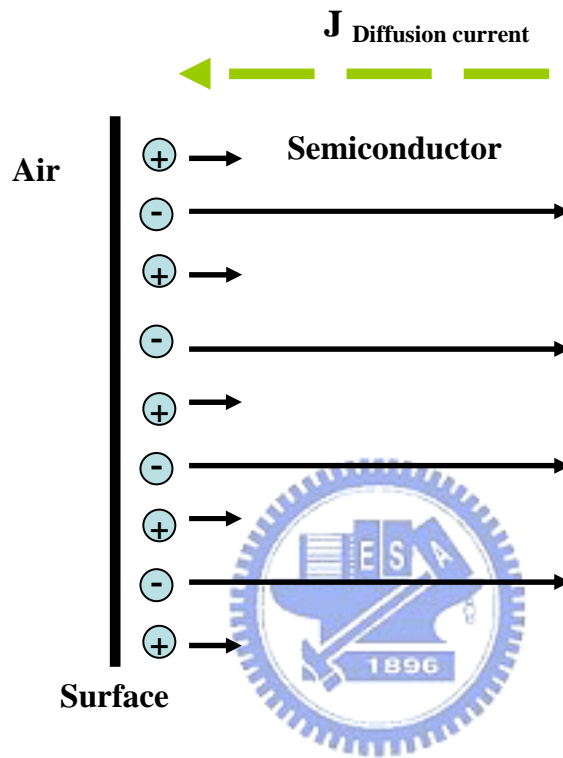
The band bending in this kind of semiconductors is not obvious resulting in a relative small surface depletion field because of comparatively small bandgap. The high absorption coefficient due to a small bandgap causes a large gradient carrier concentration after excitation by ultrafast laser pulse. The excited electrons and holes diffuse in the same direction but with different velocities, and therefore the Photo-Dember effect dominant (). Because the electron mobility is always larger than hole mobility, the photo-current is always in the same direction either n-type or p-type semiconductors. The fast photo-current rise and decay time due to semiconductors with the small electron mass and high mobility often possess fast photo-current rise and decay time that is helpful for efficient THz generation. In this mechanism the need of photon energy is comparably small; therefore, the free carriers have large excess energy. The photo-Dember voltage can be expressed by [19]:

$$V_D = \frac{k_B(T_e b - T_h)}{e} \frac{1}{b+1} \ln\left(1 + \frac{(b+1)\Delta n}{n_0 b + p_0}\right) \quad (2-1-3.1)$$

Where n_0 and p_0 are the intrinsic concentration of the electrons and holes, b is the mobility ratio $b = \frac{\mu_e}{\mu_p}$, and T_e and T_h are the temperature of photo-excited electrons and holes, respectively. From Eq (2-1-3.1) several properties can be concluded: The conditions to enhance the Photo-Dember voltage are high electron temperature, mobility ratio b and low intrinsic carrier concentration. The corresponding electric field ($E_D = V_D/d$, d is absorption length) is enhanced by decreasing absorption length. Thus, the Photo-Dember effect is much stronger in narrow bandgap materials (InAs) than in wide bandgap materials (GaAs). Recently, InAs has been reported as a strong THz emitter with intensity at least one order of magnitude higher than other unbiased semiconductor emitters such as InP and GaAs. Therefore, high conversion efficiency has made InAs received much attention and be one of the most widely used THz emitters. InN has also been considered to generate THz waves via Photo-Dember effect [15]. In this thesis, we would focus on the properties of terahertz emission from InN with different lattice structure.

The other band structure parameter we need to concern is the valley energy separations. If the excited carriers have excess energy higher than valley energy

separation, intervally scatterings will happen. Because of the reduction of the transient mobility in the L -valley, where the electron mobility is expected to be extremely low, the terahertz radiation from Photo-Dember effect became relatively small.



Semiconductor	E_g (eV)	$m_0^*(m_e)$	α (eV ⁻¹)	ΔE_1 (eV)	ΔE_2 (eV)
InN	0.78	0.04	1.43	1.775	2.709
InAs	0.354	0.023	1.4	0.73.	1.02

Table 2-1. Band structure parameters of InN and InAs. The effective mass m_0^* at the bottom of the valley and nonparabolicity factor α are given for the central valley. ΔE_1 (ΔE_2) is the energy separation between the central valley and first (second) satellite valley. The parameters for InN and InAs are taken from [20] [21], respectively.

2-1-4 Optical Rectification

The nonlinear optical process was first suggested by *Chuang* et al.[22][23][24].

THz radiation field generated by the optical rectification, $E_{\text{THz}}(t)$, is proportional to the second-order nonlinear polarization in the near field. In the far field, the observed THz field amplitude, $E_{\text{THz}(ob)}$, is proportional to the projection of the second time derivative of the nonlinear polarization to the polarization direction of detection, \mathbf{n} (a unit vector normal to the observation direction), at the observation point:

$$E_{\text{THz}}^{ob}(t) = \mathbf{n} \cdot E_{\text{THz}} \propto \mathbf{n} \cdot \frac{\partial^2 P(t)}{\partial t^2} \quad (2-1-4.1)$$

$$E_{\text{THz}}^{ob}(\Omega) \propto \Omega^2 \mathbf{n} \cdot P(\Omega) \quad (2-1-4.2)$$

The strong dependence of the emitted THz radiation intensity on the crystal orientation to the pump polarization is the most unambiguous evidence for the contribution of the $\chi^{(2)}$ process. By rotating a sample about its surface normal, the relative contribution of the azimuthal-angle-dependent component to the total THz radiation can be estimated.

Taking the surface normal as the X -axis and the reflection plane as the XY -plane in the laboratory frame, the nonlinear polarization induced in the semiconductor due to the optical rectification for (111) and (100) surfaces is expressed by (2-1-4.3) and

(2-1-4.4), respectively [25]: For (111) surfaces,

$$P = \begin{pmatrix} P_x(t) \\ P_y(t) \\ P_z(t) \end{pmatrix} = 2\varepsilon_0 d_{14} \langle E^2(\Omega) \rangle \begin{pmatrix} -\frac{1}{\sqrt{3}} \cos^2 \phi + \frac{2}{\sqrt{6}} \sin^2 \phi \\ \frac{2}{\sqrt{6}} \cos^2 \phi \cos 3\theta - \frac{2}{\sqrt{6}} \cos \phi \sin \phi \\ \frac{2}{\sqrt{6}} \cos^2 \phi \sin 3\theta \end{pmatrix} \quad (2-1-4.3)$$

For (100) surfaces,

$$P = \begin{pmatrix} P_x(t) \\ P_y(t) \\ P_z(t) \end{pmatrix} = 2\varepsilon_0 d_{14} \langle E^2(\Omega) \rangle \begin{pmatrix} \cos^2 \phi \sin 2\theta \\ \sin 2\phi \sin 2\theta \\ \sin 2\phi \cos 2\theta \end{pmatrix} \quad (2-1-4.4)$$

Here, ϕ is the angle between the pump-laser beam and the surface normal refracted inside the sample, θ is the azimuthal angle of the sample orientation around the X-axis(See Fig 2-2.) and $d_{14} = \chi_{14}^{(2)} / 2$ is the nonlinear susceptibility coefficient for the difference frequency, Ω , in the contracted notation, and $\langle E(\Omega) \rangle$ is the autocorrelation function of $E(\omega)$. Using (2-1-4.1) and considering the refraction at the interface between the semiconductor/air interfaces, the p -polarized THz field amplitude observed in the direction of optical reflection is given by the following equation:

$$E_{THz}^{ob} \propto \hat{n} \cdot P = (-\sin \phi_{THz}, \cos \phi_{THz}, 0) \begin{pmatrix} P_X \\ P_Y \\ P_Z \end{pmatrix} \quad (2-1-4.6)$$

$$= -P_X \sin \phi_{THz} + P_Y \cos \phi_{THz}$$

The refraction angles for the optical and THz beams are determined by the generalized Snell's law as : $\sin 45^\circ = n_{opt} \sin \phi = n_{THz} \sin \phi_{THz}$, where n_{opt} and n_{THz} is the refractive index for the pump laser and THz radiation in the semiconductor, respectively. The azimuthal angle dependence of THz radiation amplitude from semiconductors with n-InAs (111) and n-InSb (100) are shown on Fig 2-3.

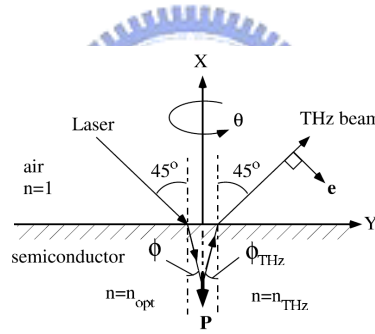


Fig 2-2 Optical geometry of THz radiation from a semiconductor surface [25]

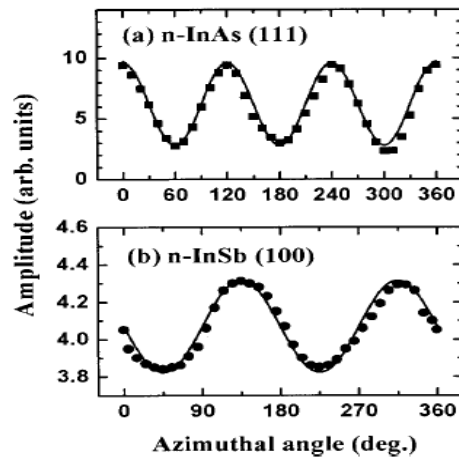


Fig 2-3 Azimuthal angle dependence of THz radiation amplitude from semi-conductors with (a) n-InAs (111) and (b) n-InSb. [25]

2-1-5 THz Enhancement by External Magnetic Field

In past years, several groups have observed a large magnetic field induced the enhancement in surface-field THz emission from a variety of semiconducting materials (GaAs, InAs, InP, GaSb and InSb). In the paper published by M. B. Johnston et. al.[30], they build up a Monte Carlo dynamics model to explain the phenomenon of magnetic-field enhancement of THz emission and the schematic diagram of the experiment geometry is shown on Fig 2-4. The carrier motion is:

$$\vec{a}_i(t) = \frac{q_i}{m_i^*} [\vec{E}(\vec{r}_i, t) + \vec{v}_i(t) \times \vec{B}] \quad (2-1-5.1)$$

$$\frac{\partial \vec{J}}{\partial t} = \sum_i q_i \vec{a}_i \quad (2-1-5.2)$$

where \vec{r}_i is the position of the carrier, with charge q_i and effective mass m_i^* , in an electric field $\vec{E}(\vec{r}_i, t)$ and applied magnetic field \vec{B} . In the absence of any magnetic field there are no x or y components of the average current, because the system has rotational symmetry about the z axis. Hence, a simple linear THz dipole is formed in the z direction. The magnetic field rotates the dipole, producing x and y components of similar magnitude to the z component.

The THz radiation emitted by the dipole is transmitted through the semiconductor surface, and the enhanced power recorded in the experiments is a

result of a dramatic increase in transmission when the dipole is rotated. The TE and TM fields inside the semiconductor are obtained from $\mathbf{J}(t)$, and the external fields computed using the Fresnel transmission coefficients for the two polarizations :

$$E_{\text{TE}}(\theta_e, t) \propto \frac{2\sin\theta_e \cos\theta_i}{\sin(\theta_e + \theta_i)} \left[\frac{\partial J_y}{\partial t} \right] \quad (2-1-5.3)$$

$$E_{\text{TM}}(\theta_e, t) \propto \frac{4\sin\theta_e \cos\theta_i}{\sin 2\theta_e + \sin 2\theta_i} \left[\frac{\partial J_z}{\partial t} \sin\theta_i - \frac{\partial J_x}{\partial t} \cos\theta_i \right] \quad (2-1-5.4)$$

where θ_i is the corresponding internal angle, given by Snell's law, $n_e \sin\theta_e = n_i \sin\theta_i$, with n_e, n_i the external and internal refractive indices, respectively. At $B=0\text{T}$, there is a strong suppression of the TM polarized bow-tie dipole pattern due to the index of semiconductor (GaAs: $n_i=3.5$). It is less than 17° of the internal angle, so, only few fraction of the emission close to the dipole axis (z-axis) can pass through the surface.

For $B=8\text{T}$, the dipole is rotated by the magnetic field, thus, the magnetic field enhancement can be seen to be in reality a reduction of the suppression of the emission from the z polarized dipole. The theory predicts a TM power enhancement of ~ 10 -fold, and a total enhancement (TE+TM) of ~ 15 -fold. The corresponding experimental enhancements are ~ 20 and 30 times.

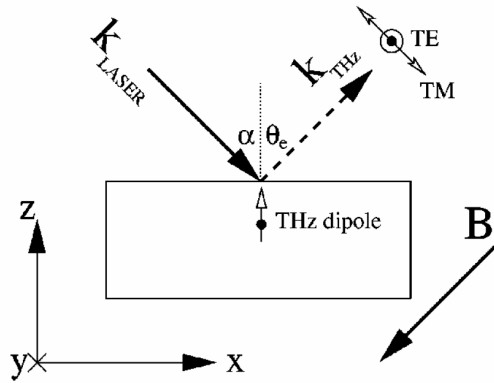


Fig 2-4. Schematic diagram of the experimental geometry and coordinate system.[30]

2-2 Terahertz Detection: Electro-Optical Crystal and Free Space Electro-Optic Sampling (FS-EOS)

The coherent detection of a THz-pulse beam with EO crystals is based on the linear Electro-Optical effect (Pockels effect). It is a phase-sensitive detection of electromagnetic (EM) radiation based on a birefringence in an EO crystal induced by the incident EM radiation. Under the external field, the refractive index of a certain material can be changed with the field intensity. In 1996, X. C. Zhang found that THz pulse can be detected by electro-optic sampling methods [6]. The THz electric field would modulate the birefringence of the EO crystals and then change the polarization ellipticity of the optical probe beam passing through the crystal with the time delay. The refractive-index-ellipsoid modulation of the optical beam can then be analyzed to provide the information of the amplitude and phase of the applied electric field.

When using an amplified laser system, the THz pulses are best detected via free

space electro-optic sampling rather than photoconductive antenna, because the need of focused beam is not necessary that decrease the potential for damaging the material. It is a non-resonant method and is suitable for broadband detection [26]. The THz beam is focused onto an EO crystal and modify the index ellipsoid transiently via Pockels effect. The linearly polarized laser probe beam propagate inside the crystal combined with the THz beam, and its phase is modulated by the refractive index change induced by the electric field of the THz pulse as shown in Fig 2-5. The signal difference is proportional to the phase change Γ induced by THz field, for EO crystal, the phase retardation induced in the EO crystal is given by the following equation change term

Γ can be expressed by

$$\Gamma = \frac{\pi d n^3 \gamma_{41}}{\lambda} E \quad (2-2.1)$$

Where d is the thickness of the crystal, n is the refractive index of the crystal at the wavelength of the near-infrared (NIR) probe beam, λ is the probe beam wavelength, γ_{41} is the Electric-Optic coefficient, and E is the electric field of the THz wave. Thus, we can obtain the entire THz time-domain waveform by measuring the signal difference via a balance detector as a function of delay time between the THz pulse and the probe pulse. The total frequency response of the EO sampling technique is given by the product of (2-2.1) and the following equation:

$$G(\omega) = \frac{T(\omega)}{\delta(\omega)} \int_0^{\delta(\omega)} \exp(i2\pi\omega \cdot t) dt = T(\omega) \frac{\exp[i2\pi\omega\delta(\omega)] - 1}{i2\pi\omega\delta(\omega)}$$

$$\delta(\omega) = \frac{n_g(\lambda_0) - n(\omega)}{c} d \quad (2-2.2)$$

where $n_g(\lambda_0)$ is the group refractive index at the wavelength of the probe beam, and $n(\omega)$ is the refractive index at the frequency of the incident THz radiation. $T(\omega) = 2/[n_{\text{THz}}(\omega)+1]$, is the Fresnel transmission coefficient with the refractive index of the EO crystal $n_{\text{THz}}(\omega)$ in the range of the target THz frequency. Therefore, a thicker crystal produces a greater interaction length, but on the other hand it reduces the detection bandwidth due to group-velocity mismatch.

For the time being, there are many different materials for EO sampling such as ZnTe, GaP, GaSe and InP. In addition, ZnTe and GaP are the most commonly used material for EO detection from sub-THz to several tens of THz, because of their relative large EO coefficient and they are transparent at the wavelength of the incident THz radiation. Furthermore, for high chopping frequency, EO sampling has a high SNR as well as photoconductive sampling, but it is more sensitive to laser noise.

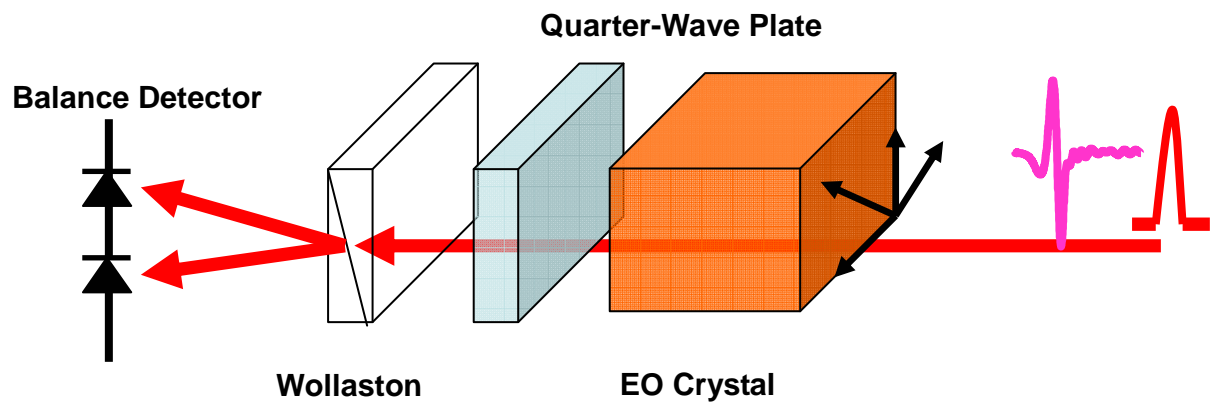


Fig 2-5 Schematic figure of Electro-optic sampling



Chapter 3 Experimental Setups

In this chapter, we will briefly describe our femto-second laser system in section 3.1 and introduce the THz time-domain spectroscopy (THz-TDS) systems in section 3.2.

3-1 Introduction of Femtosecond Laser System

Our femtosecond later system is shown in Fig 3-1. We use the Ti:Sapphire laser as the seeding laser which is then directed into the Ti:Sapphire regenerative amplifier (Spitfire, Spectra-Physics) for amplification. The pump laser of Spectra Physics Tsunami laser is a 5W frequency doubled diode-pumped Nd:YLF laser (Millennia V, Spectra-Physics) with a wavelength $\lambda=532$ nm. The Ti:Sapphire laser provides an output trace of intense 35fs pulses with wavelengths ranging from 750nm to 850nm. The pulse repetition rate is ~82 MHz and the output power can up to 0.4W. The properties of these two laser systems are shown in Table 3-1. Properties of Tsunami laser and Ti:Sapphire regenerative amplifier..

The pump laser for the amplification process in Spitfire is Q-switched Nd:YLF laser which delivers a high power output of 20W at 527 nm. The Spitfire amplifies the seeding pulses by a million times from 6 nJ of energy per pulse to 2 mJ per pulse. The pulse repetition rate is 1 kHz and the output power is about 2W.

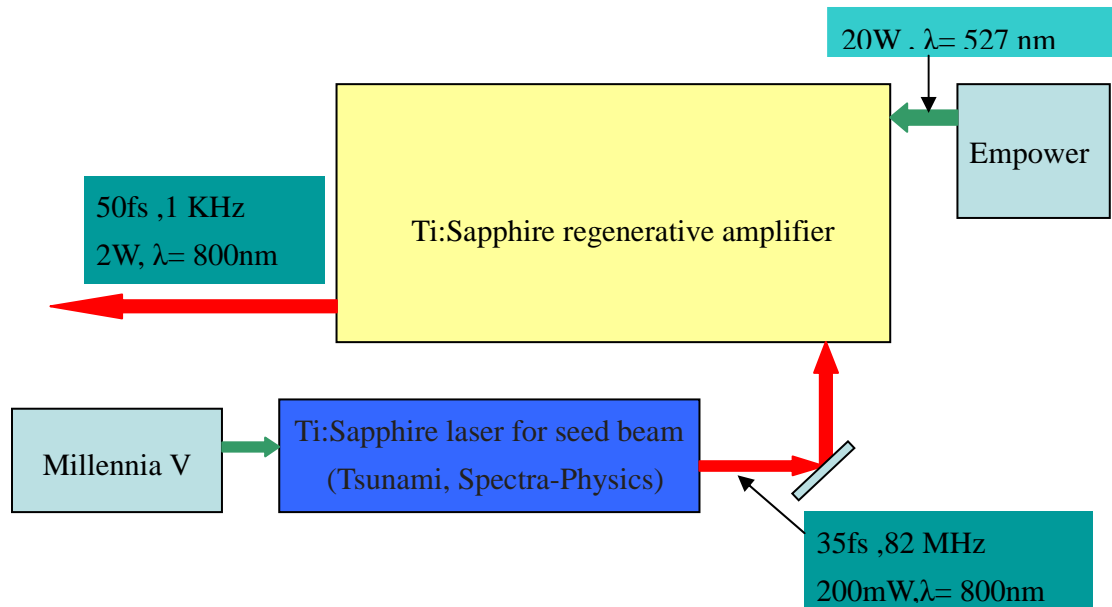


Fig 3-1. Femtosecond laser system includes Tsunami, Spitfire and two pump laser (Millennia V and Empower).

	Tsunami laser	Ti:Sapphire regenerative amplifier
Wavelength	800 nm	800nm
Pulse width	35 fs	50fs
Repetition rate	82 MHz	1kHz
Energy	0.6 nJ	2mJ
Polarization	Vertical, linear	Horizontal, linear

Table 3-1. Properties of Tsunami laser and Ti:Sapphire regenerative amplifier.

3-2 Electro-Optic THz System

The optical setup of the Electro-Optic THz system is shown in Fig 3-2. An amplified Ti:Sapphire laser providing 50fs, 800nm, 2mJ pulsed at repetition rate of 1kHz is used to drive this system. The linearly s-polarized incident beam is divided into two separated beams by a beam splitter. The transmitted beam from the beam splitter is used as pump beam to excite carrier in our samples and generate terahertz pulse. The other beam, reflected beam, is used as the probe beam to detect terahertz pulse signal. There is a half-wave plate in order to rotate the polarization of the pump beam to linearly p-polarized. Therefore, we could generate linearly p-polarized THz pulsed in a semiconductor surface emitter such as InAs at the incident angle of 70 degrees to the surface normal which is close to the Brewster angle. We use a teflon sheet which has a high transmissive characteristic in the terahertz region to block any reflected laser beam from the emitter.

The generated THz radiation is collimated and focused onto the sample by a pair of gold-coated off-axis parabolic mirrors with focal lengths of 3 and 6 inches respectively. The transmitted THz radiation is again collimated and focused onto a 2-mm-thick (110) ZnTe crystal for free space electro-optic sampling by another pair of parabolic mirrors with the same focal lengths with previous pair. A pellicle beam splitter which is transparent to the THz beam and has a reflectivity of 5% for 800nm

light is used to make the probe beam collinear with the THz beam in the ZnTe crystal.

The time delay of the probe beam, which can be tuned by the motor stage, is guided to the ZnTe crystal and the terahertz pulse collinearly impinged on it. The linear polarization of the probe beam is perpendicular to the polarization of the THz beam and we adjust the azimuth angle of the ZnTe crystal to achieve the highest modulation efficiency.

Polarization of the probe beam modulated by the THz radiation is converted to ellipsoid polarization by a quarter-wave plate. The transmitted laser pulse with polarization changed by electro-optical effect is separated into two beams with orthogonal polarizations by Wollaston beam splitter. These two beams are coupled to a balanced detector with two silicon photodiodes which is used to detect the differential signal between two individual probe beams and the signal is proportional to the THz electric field. A motor stage within the probe beam path is used to scan the delay time between the probe pulse and the THz pulse imposing on the ZnTe crystal to obtain the entire THz time-domain waveform. Connecting signal from the balance detector to a lock-in amplifier, the signal can be easily analyzed by a computer.

In order to reduce the water vapor absorption and increase the signal to noise ratio, an optical chopper and a lock-in amplifier are used. Otherwise, the entire THz beam path is also located in a closed acrylic box for nitrogen purge. An example of a

terahertz pulse with its corresponding spectrum under humidity of 55% and 5% generated by this setup is shown in Fig 3-3 and Fig 3-4

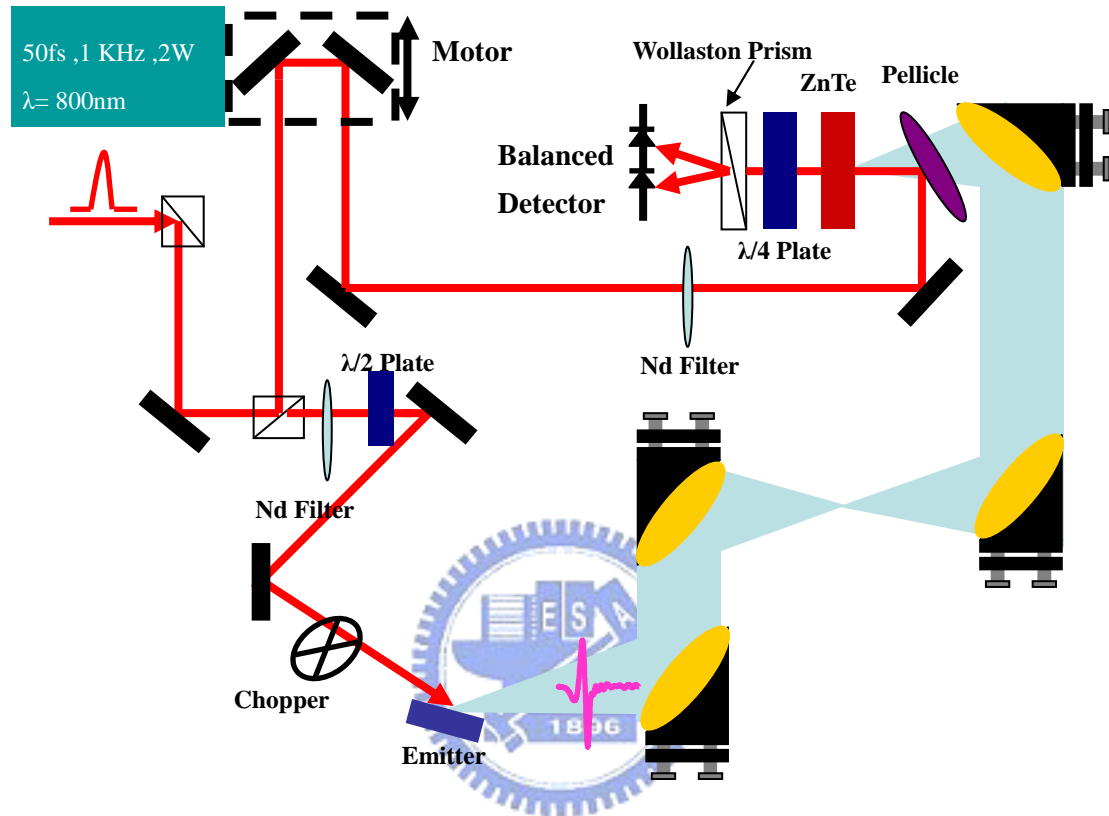


Fig 3-2. Electro-Optic THz system

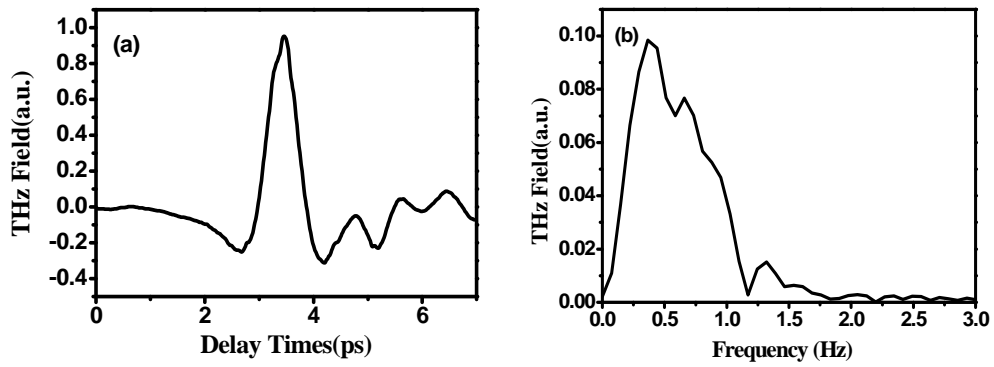


Fig 3-3. THz time-domain (a) waveform and (b) its corresponding spectrum generated by the electro-optic THz system using a-plane InN as emitter under the humidity of 55%

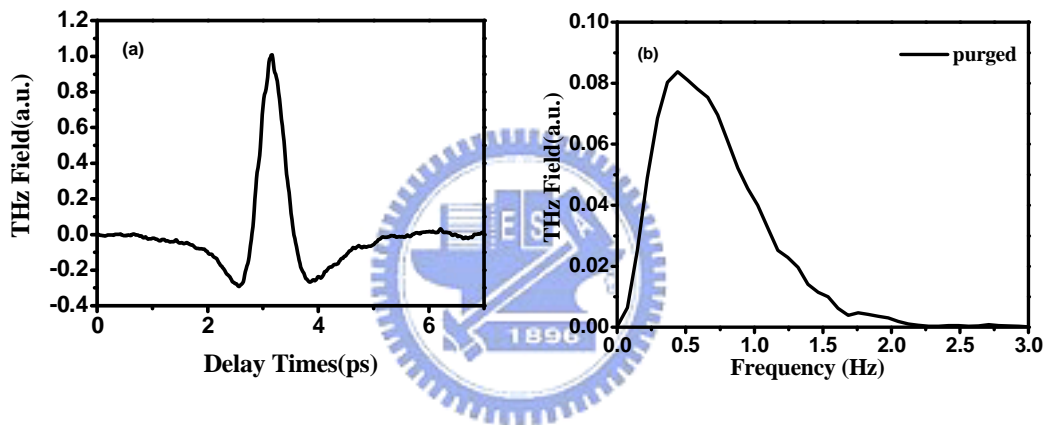



Fig 3-4. THz time-domain (a) waveform and (b) its corresponding spectrum generated by the electro-optic THz system using a-plane InN as emitter under the humidity of 5%

Chapter 4 Sample Properties

Indium nitride (InN) is an interesting and potentially important semiconductor material with superior electronic transport properties. Compared to all other group-III nitrides, InN possesses the lowest effective mass, the highest mobility, and the highest saturation velocity. Therefore, it is very suitable for high speed and high frequency electronic device applications.

The important properties of InN are lowest effective mass (high mobility), highest saturation speed in III-Nitrides, and the energy bandgap $\sim 0.65\text{eV}$ founded in 2002. Furthermore, the energy gap to the next peak of InN is 2.8eV . This property could prevent the intervalley scatterings of the electrons.



Material	Bandgap	Distance to next peak
InAs	0.35eV	0.73eV
InSb	0.17eV	0.51eV
Gasb	0.73eV	0.08eV
InP	1.34eV	0.49eV
GaAs	1.42eV	0.29eV
InN	0.69eV	2.8eV

Table 4-1. The bandgap energies of some semiconductors.[16]

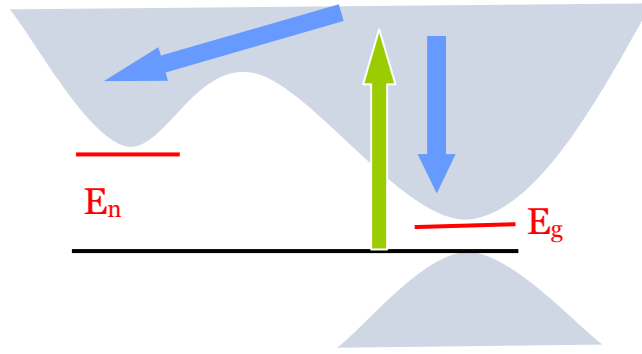


Fig 4-1 Simplified view of the band edge structure of InN.

Properties	GaN	AlN	InN
Effective electron mass	0.2m ₀	0.48m ₀	0.07m ₀
300k mobility (cm ² /Vs)	1000	300	4000
Saturation speed (10 ⁷ cm/s)	2.9	1.7	4.2

Table 4-2. Properties of the III-Nitride compound semiconductors

Due to poor sample quality, about few years ago, no band-edge photoluminescence (PL) spectra were reported. In fact, the previous band gap value of ~1.9 eV was determined in the early studies mainly by interband absorption measurements performed on InN polycrystalline films deposited by sputtering techniques, in which oxygen incorporation is a severe problem. The epitaxial growth of InN films is very difficult because of the extremely low dissociation temperature (causing instability in stoichiometry at high temperatures) of InN and the lack of suitable matched substrates

in terms of lattice constants and thermal expansion coefficients. Recent progress in epitaxial growth techniques (most notably molecular-beam epitaxy (MBE) using highly active nitrogen plasma) [36][37][38][39][40] has led to significantly improved InN samples, which show PL as well as a clear absorption edge at $\sim 0.7\text{--}0.9$ eV[36][38][41].

In this thesis report, the two different samples we used are c-plane InN epilayer and a-plane InN epilayer. We describe the growth method and electric properties of these two samples in the next sections.

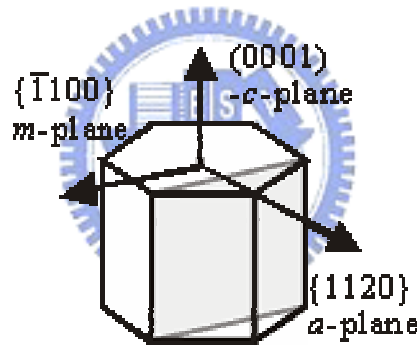


Fig 4-2. Crystal structure of InN

4-1 InN Film (c-plane InN)

For this work, one of the samples, the InN film(c-plane InN), was grown on the Si (111) substrate using a double-buffer technique by plasma-assisted molecular-beam epitaxy (PA-MBE). The InN epilayers were grown on Si(111) using the epitaxial AlN/ β -Si₃N₄ double-buffer layer technique. Details of the growth procedure can be found elsewhere.[24] Silicon is a suitable substrate material for InN heteroepitaxy

because of the smaller lattice mismatch of $\sim 8\%$ for InN(0001)/Si(111) compared to $\sim 25\%$ for InN(0001)/Al₂O₃(0001).

This *c*-plane InN film was not intentionally doped, the typically display residual *n*-type conductivity. The thickness of the *c*-plane InN film is about 1.05 μm . By room-temperature Hall effect measurement, the free electron concentration and mobility which have been determined are $3.1 \times 10^{18} \text{ cm}^{-3}$ and $1036 \text{ cm}^2/\text{Vs}$, respectively.

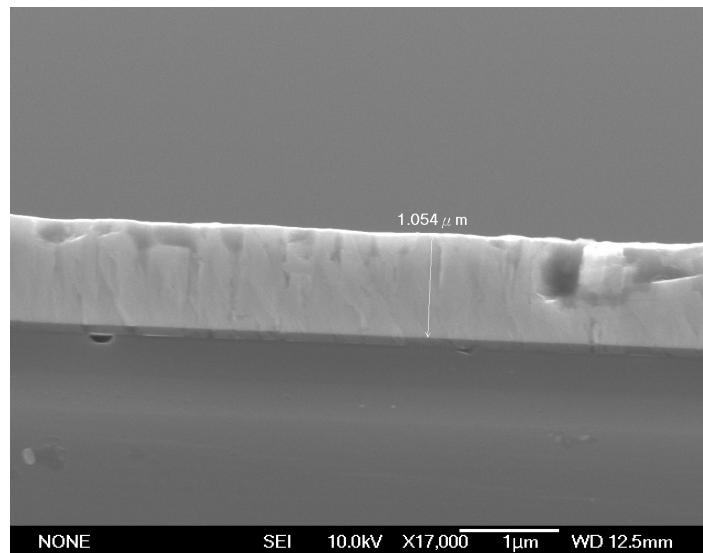


Fig 4-3 The SEM pictures of *c*-plane InN film. [This picture is taken from the Prof. S. Gwo's group, The Department of Physics, National Tsing Hua University.]

4-2 Nonpolar InN Film (*a*-plane InN)

From the letter published by Hai Lu.[42], the comparison of the electrical properties of *a*-plane and *c*-plane InN films were reported [42]. Fig 4-4 shows the RT Hall mobility and carrier concentration of the *a*-plane InN films as a function of film thickness. The inset of this figure shows the corresponding data of the *c*-plane films. It

is found that under current growth conditions, increasing film thickness does not lead to an apparent improvement on electrical properties of the *a*-plane InN. In the thickness range between 0.5 and 3 μm , its Hall mobility and carrier concentration fluctuate around $250 \text{ cm}^2/\text{Vs}$ and $6 \times 10^{18} \text{ cm}^{-3}$, respectively. This behavior is quite different from that of *c*-plane InN. As shown in the inset, with increasing film thickness, the Hall mobility of *c*-plane InN will continuously increase while carrier concentration decreases.

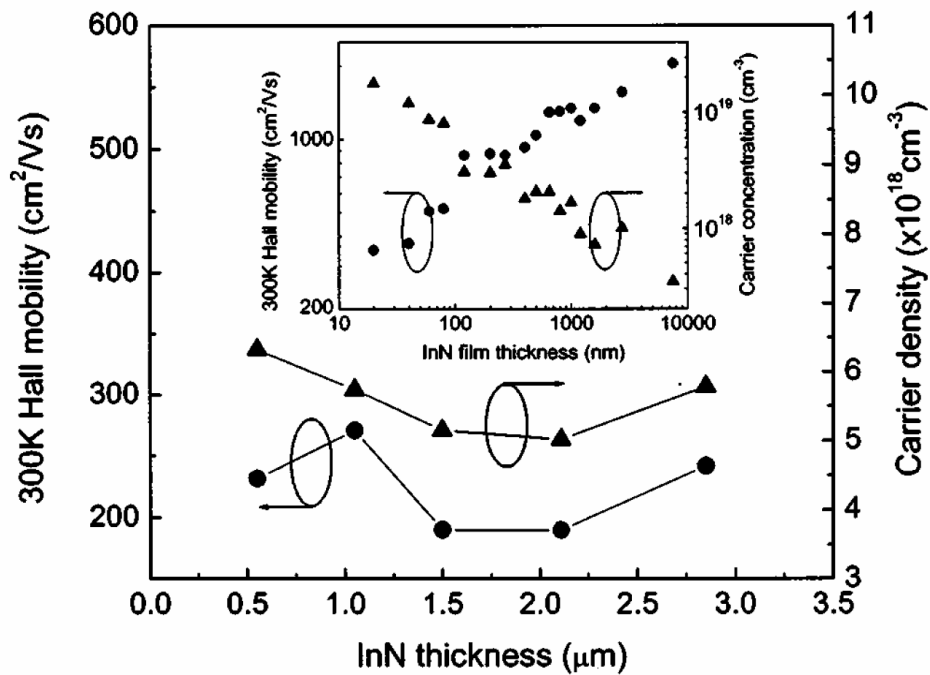


Fig 4-4. RT Hall mobility and carrier concentration of *a*-plane InN films as a function of film thickness. The inset shows the corresponding data of the *c*-plane InN films. [41]

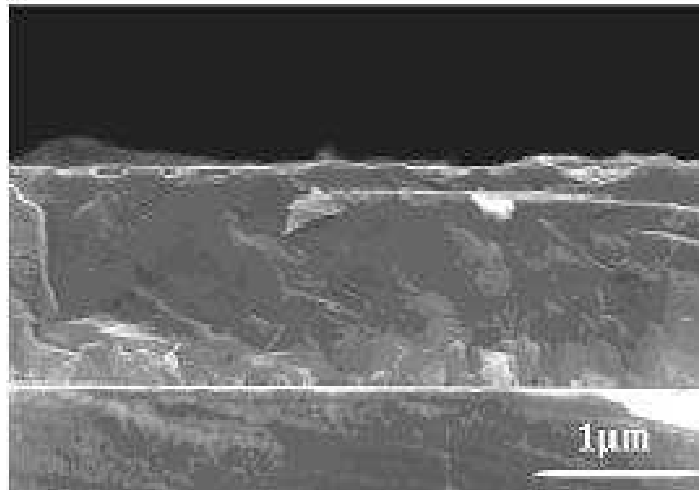


Fig 4-5. The SEM pictures of a-plane InN film. [This picture is taken from the Prof. S. Gwo's group, The Department of Physics, National Tsing Hua University.]



Chapter 5 Experimental Results and Discussion

In this chapter, we first discuss the results of a significant enhancement in terahertz emission from the indium nitride (InN) films grown along the a-axis (a-plane InN), relative to the InN films grown along the c-axis. Afterward we discuss the azimuthal- and polarization angle dependence of emitted terahertz wave.

For this work, THz emission from InN was measured by electro-optic THz system describe in chapter 3. The photo-exciting beam is collimated on the samples with a spot size of ~ 2 mm diameter at the angle of incidence of 70° , which is near the Brewster angle. The emitted THz pulses were detected by free-space electro-optic sampling in a 2-mm-thick ZnTe crystal as a function of delay time with respect to the optical pump pulse.



5-1 Terahertz Emission from InN Surface

In the past years, due to the narrow directive bandgap and large energy gap to the next peak, InN becomes a potential emitter for THz emission. There have been several reports on terahertz emission from InN films[14][15][16]. From our group past research, the terahertz emission from InN film grown by molecular-beam epitaxy on Si(111) substrates has been investigated[27].

Electron accumulation layer at the surface of c-plane InN is very thin (<10 nm) and

its contribution to terahertz generation is negligibly small, therefore, the main mechanism emitted the terahertz radiation for c-plane InN film is supposed to the Photo-Dember effect introduced in the section 2-1-3. From the Eq (2-1-3.1):

$$V_D = \frac{k_B(T_e b - T_h)}{e} \frac{1}{b+1} \ln\left(1 + \frac{(b+1)\Delta n}{n_0 b + p_0}\right), b = \mu_e / \mu_p \quad (2-1-3.1)$$

This equation tell us that the Photo-Dember effect is enhanced by larger electron mobility ($\mu_e \propto b$), and higher electron excess energy ($\propto T_e$). In other words, the narrow-bandgap semiconductors have the preferred conditions necessary to create a large photo-Dember field, that is, the very large electron mobility and large excess carrier energy. Moreover, the photo-Dember field (V_D/d , d : absorption depth) in narrow-bandgap semiconductors is further enhanced by the small absorption depth. On the other hand, the surface-depletion field is expected to be small because of the small bandgap energy, in contrast to the wide bandgap semiconductors.

Because the electron accumulation layer at the surface of n-type InAs and c-plane InN is very thin, its contribution to terahertz generation is negligibly small. It is concluded that the terahertz emission mechanism of both materials is the photo-Dember effect, however, the terahertz radiation emitted from c-plane InN films is typically one order of magnitude weaker than that from InAs.(The emission amplitude from n-type InAs is larger than c-plane InN film at least 30 times.) Through

the explanation of the mechanism for photo-Dember effect, we have known that this enormous difference in terahertz radiation amplitude ought to result from the dissimilarity of electron mobility and direct bandgap with these semiconductors: The electron mobility(μ_e) of n-type InAs is about 30000 cm²/Vs, but that of c-plane is only 1036 cm²/Vs. Furthermore, from the pump source of our experiments with $\lambda = 800\text{nm}$ (photon energy =1.55eV), the excess energy(ΔE) of these samples are 1.19 eV for InAs and 0.76 eV for c-plane InN, respectively.

In the other hand, we find that the THz emission from the InN film grown along the a-axis (a-plane InN) is stronger than that from the InN film grown along the c-axis (c-plane InN) about one order (Fig 5-1). The photo-excited carriers generated close to the surface of semiconductors can be accelerated by an appropriate electric field and the resultant transient electric dipole can lead to generation of terahertz pulses. It is well known that the contribution of electron accumulation field to terahertz emission would be very small for both *c*- and *a*-plane InN due to the narrow thickness of the electron accumulation layer. For the photo-Dember effect, which is proportional to electron mobility and is independent to the crystal growth direction, its contribution to the radiation from *a*-plane InN ($\mu = 298 \text{ cm}^2 / \text{V}$) is even smaller than that from *c*-plane InN($\mu = 1036 \text{ cm}^2 / \text{V}$). Therefore, the drastic power enhancement observed for *a*-plane InN cannot be explained by either the electron accumulation field or the photo-Dember



fields.

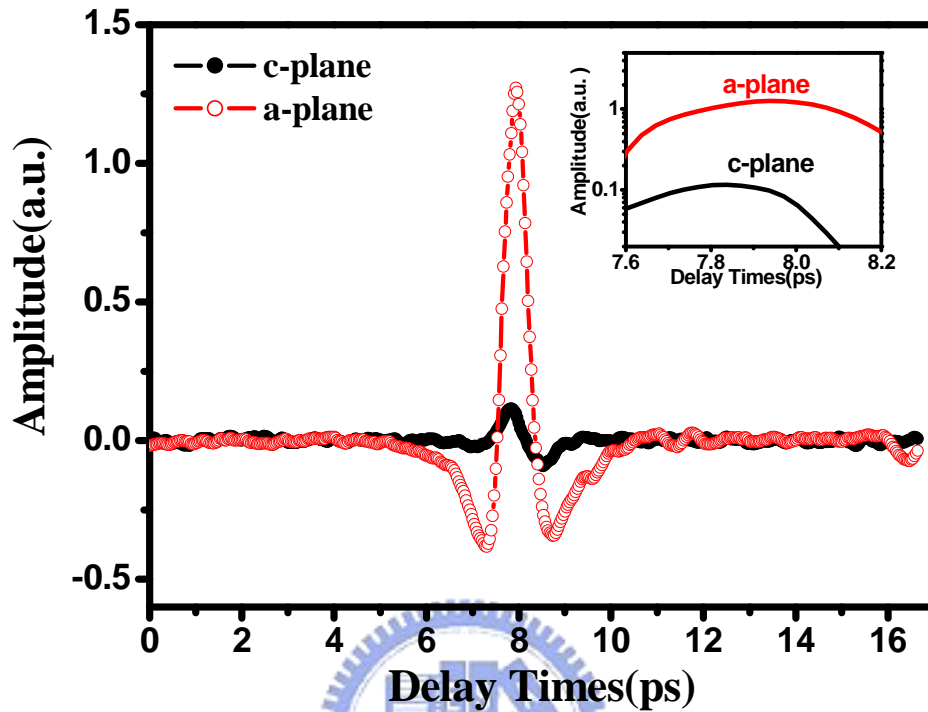


Fig 5-1 The amplitude of the terahertz emission from a-plane InN film (red square) compare to that from c-plane InN film(black circle). The excitation is 0.24 mJ/cm^2 . Inset: comparison between a-plane InN , c-plane InN measure under identical experimental condition.

From the past investigations, the most familiar method to improve the THz radiation is using an external magnetic field[28][29]. In past years, several groups have observed a large magnetic field induced enhancement in surface-field THz emission from a variety of semiconducting materials (GaAs, InAs, InP, and InSb)[44][45][46]. In the paper published by M. B. Johnston et. al.[30], they build up a Monte Carlo dynamics model to explain the phenomenon of magnetic-field enhancement of THz emission and the schematic diagram of the experiment geometry

is shown on Fig 5-2. Because of the rotational symmetry about the z axis, there are no x or y components of the average current in the absence of any magnetic field. Hence, a simple linear THz dipole is formed in the z direction like Fig 5-3(a). The magnetic field rotates the dipole, producing x and y components of similar magnitude to the z component (see Fig 5-3(b)).

The THz radiation emitted by the dipole is transmitted through the semiconductor surface, and the enhanced power recorded in the experiments is a result of a dramatic increase in transmission when the dipole is rotated. Using the Fresnel transmission coefficients for the two polarizations, the external fields are:

$E_{TE}(\theta_e, t) \propto \frac{2\sin\theta_e \cos\theta_i}{\sin(\theta_e + \theta_i)} \left[\frac{\partial J_y}{\partial t} \right]$	(2-1-5.3)
$E_{TM}(\theta_e, t) \propto \frac{4\sin\theta_e \cos\theta_i}{\sin 2\theta_e + \sin 2\theta_i} \left[\frac{\partial J_z}{\partial t} \sin\theta_i - \frac{\partial J_x}{\partial t} \cos\theta_i \right]$	(2-1-5.4)

where θ_i is the corresponding internal angle, given by Snell's law, $n_e \sin\theta_e = n_i \sin\theta_i$, with n_e, n_i the external and internal refractive indices. At $B=0T$, there is a strong suppression of the TM polarized bow-tie dipole pattern due to the index of semiconductor, for example, GaAs ($n_i=3.5$), it is less than 17° of the internal angle, so, only few fraction of the emission close to the dipole axis (z -axis) can pass through the surface. For $B=8T$, the dipole is rotated by the magnetic field, thus, the magnetic

field enhancement can be seen to be in reality a reduction of the suppression of the emission from the z polarized dipole. This theory predicts the corresponding experimental enhancements are ~ 20 and 30 times. Therefore, we could use this similar mechanism for improving light extraction efficiency to explain the THz enhancement on a-plane InN.

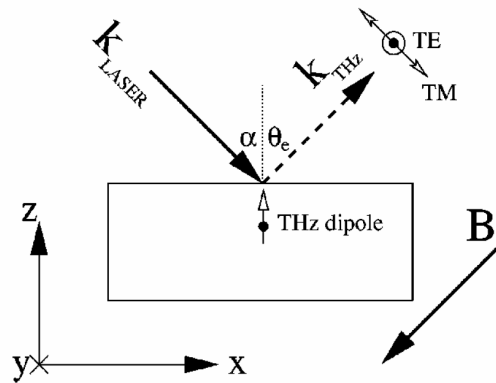


Fig 5-2 Schematic diagram of the experimental geometry and coordinate system.[30]

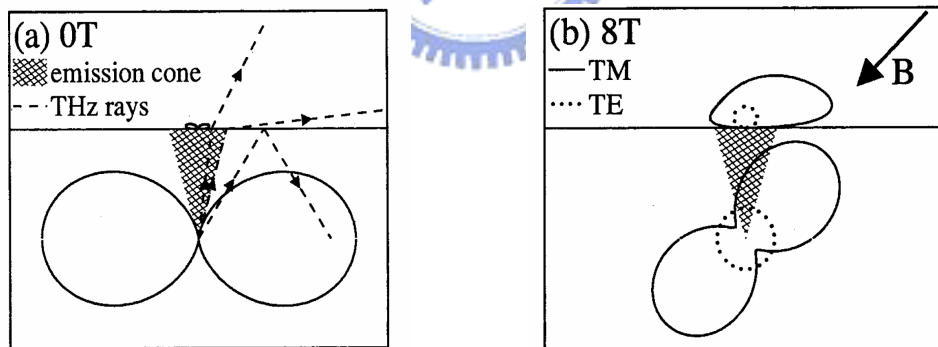


Fig 5-3 Calculated polar radiation patterns for GaAs at (a) 0 and (b) 8 T. In each part the horizontal line is a schematic representation of the surface of the semiconductor. The bow-tie pattern below the surface line is calculated for radiation within the semiconductor, whereas the pattern above the surface shows the radiation emitted into free-space. The vector B indicates the magnetic-field direction. [30]

In the c-plane InN film, the stacking series of its wurtzite structure is ABABAB...along the c-axis direction so that there are either In- or N-terminated polar surfaces in the surface layers of c-plane InN. This structure results in a electric field generated by these In-N layers directly perpendicular to the surface. For this reason, the out-of-surface radiation would be significantly limited by the geometrical structure which be mentioned before. There would be only few percentages of the radiated terahertz power from this dipole able to escape the surface due to the small emission cone derived from the total reflection within a material of high refractive index. From the other point of view, the layers of a-plane InN have the same amount of In and N atoms in a plane and the in-plane In-N dimers form an in-plane intrinsic electric field perpendicular to the a-axis(see Fig 5-4). Due to the terahertz dipole formed in the favorable in-plane direction, we could expect that the a-plane InN could create the enhancement of terahertz radiation as much as the method with external magnetic field. In spite of the same order of the THz power enhancement, with the magnetic-field-assisted method, it needs to use an awkward experimental setup. In comparison, the power enhancement from a-plane InN just depend on the growth direction so that it can be a general phenomenon for semiconductors grown in the nonpolar direction.

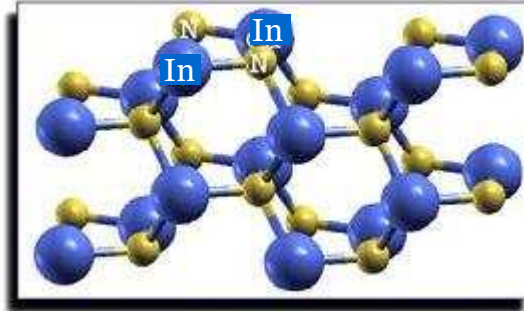


Fig 5-4 Ball-and-stick model of the a-plane surface. Large balls are In, small balls are N. [47]

We measured the reflectivity of these samples and the result is shown in Fig 5-5.

The reflectivity of a-plane InN is bigger than that of c-plane one a little bit. Furthermore, pump fluence dependence in Fig 5-6 shows that when the pump fluence is increased 10 times, the amplitude of THz emission from a-plane InN film is enhanced by 2.5 times, but that of c-plane InN film is by 1.8 times.

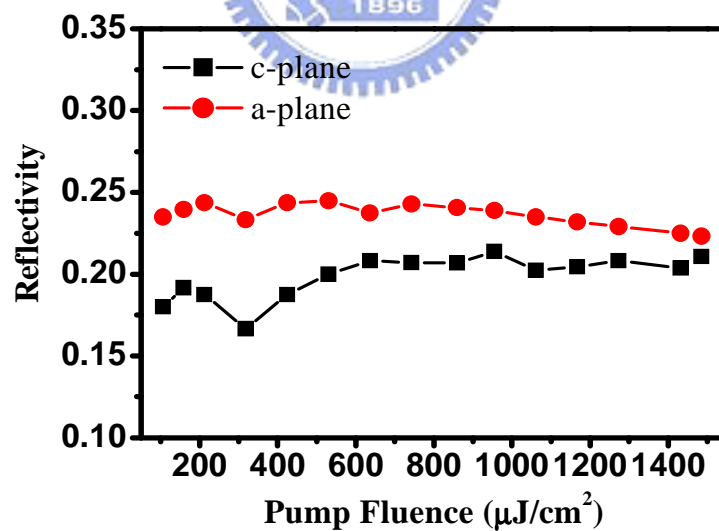


Fig 5-5 Optical reflectivities in InN-epilayer and nonpolar InN as a function of excitation energy. Optical absorption in InN film is about 80%, while that in nonpolar InN is about 76%.

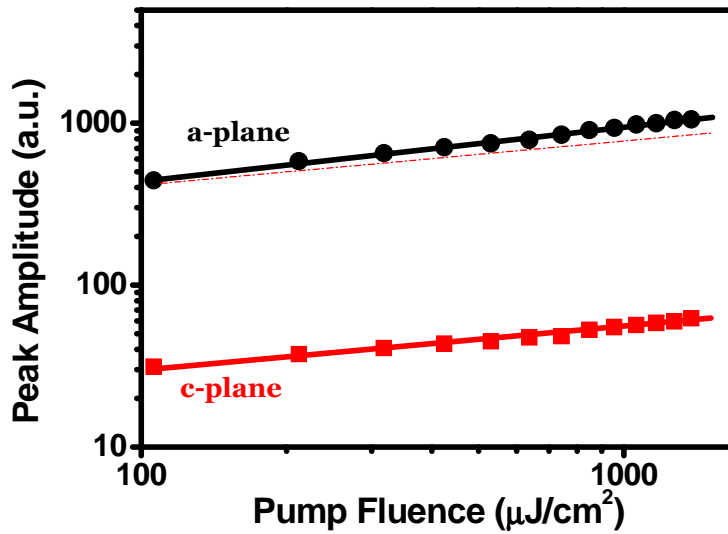


Fig 5-6. Peak amplitude of terahertz emission for c-plane InN film (red points) and a-plane InN film (black points) as a function of laser pump power.



5-2 Azimuthal Angle dependence of InN

In the section 2-4 we have shown the optical rectification effect of some semiconductor. This effect of InAs and InN will be shown by detail in this section. See the Fig 5-7, The nonlinear contribution is proportional to the azimuthal angular modulation of $\sin 2\theta$ with a small DC offset for (100)-oriented n-InAs. This phenomenon could be derived by the theory discussed in Section 2-1-4 :

$$\begin{aligned}
 E_{THz}^{ob} &\propto \hat{n} \cdot P = (-\sin \phi_{THz}, \cos \phi_{THz}, 0) \begin{pmatrix} P_X \\ P_Y \\ P_Z \end{pmatrix} \\
 &= -P_X \sin \phi_{THz} + P_Y \cos \phi_{THz}
 \end{aligned}
 \tag{2-1-4.6}$$

For the pump-laser wavelength of 800 nm, ϕ is 10.9° and 9.0° for InAs and InSb respectively. For THz radiation, ϕ_{THz} is estimated to be 10.9° and 21.5° for InAs and InSb respectively. Using this value, the azimuthal angle dependence of the radiation amplitude due to optical rectification can be written as follows:

$$E \propto (0.773 \cos 3\theta - 0.153) d_{14} \quad \text{for (111) InAs} \quad (2-1-4.8a)$$

$$E \propto 0.182 \sin(2\theta) d_{14} \quad \text{for (100) InAs} \quad (2-1-4.8b)$$

$$E \propto -0.069 \sin(2\theta) d_{14} \quad \text{for (100) InSb} \quad (2-1-4.8c)$$

In Fig 2-3, the nonlinear effect contribution is proportional to azimuthal-angle dependent modulation of $\cos 3\theta$ for (111)-oriented InAs, and $\sin 2\theta$ for (100)-oriented InAs[25].

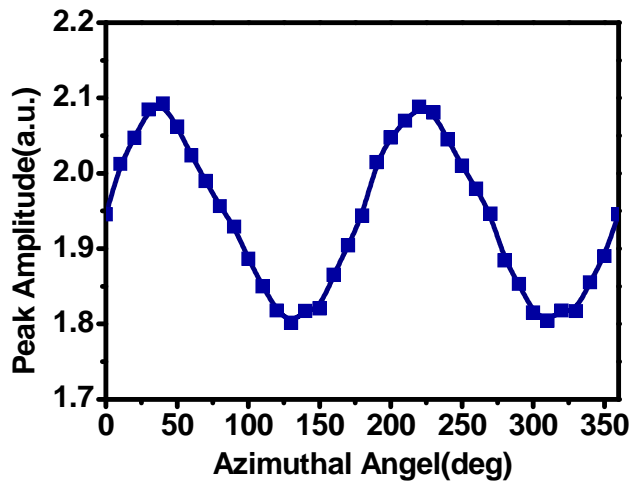
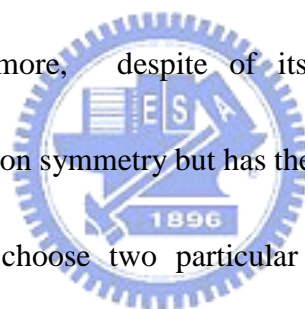


Fig 5-7. Azimuthal-angle dependence of THz-emission amplitude from n-InAs

The azimuthal angle dependence of p- and s- polarized terahertz fields are measured as the InN samples are rotated about surface normal. The azimuthal angle dependence measurement in Fig 5-8(b) shows that terahertz emission from a-plane InN has a strong angle-independent response superimposed with a relatively weak angle-dependent component with the fourfold symmetry. We propose that the dominant azimuthal-angle-independent response is resulted from the accelerated photo-carriers with the in-plane electric field of the a-plane InN film, while angle-dependent radiation might be due to nonlinear optical process. The apparent angular dependence of the terahertz signal from a-plane InN is quite different from terahertz emission from the c-plane InN, which exhibits no significant angular dependence (<5% of total amplitude) as shown in Fig 5-8(a). A similar fourfold azimuthal angle dependence has been observed for weakly excited (100) InAs under an external magnetic field, which is proposed to be due to an anisotropic intervalley scattering in four equivalent direction [31]. However, the intervalley scattering for InN should be quite small because the excess energy of ~1.55eV pump laser over its bandgap energy is much smaller than the energy gap between the conduction band minimum and the next local minimum [32]. Therefore, we could rule out this mechanism. Nonetheless, the detailed knowledge of the nonlinear tensor elements of the a-plane InN has not yet been known. In this region, it needs some effort in study about the detailed structure of this material to clarify the

mechanism of azimuthal angle dependence.

Fig 5-9. Peak amplitude of the p-polarized terahertz fields as function of azimuthal angle rotation of a-plane InN film excited at different fluence (a) 20mW (b) 50mW (c) 75mW (d) 100 mW by p-polarized pump beam. shows the azimuthal angle dependent THz emission from a-plane InN measured at different pump power. As the pump power increases from 25mW to 100mW, the ratio of the angular-dependent term to the angular-independent term is increased from 10% to 20%. It may imply that the increase of contribution of nonlinear process to THz emission would relate to the pump fluence. Furthermore, despite of its small amplitude, s-polarized component has the same rotation symmetry but has the opposite polarity relative to the p-polarized component. We choose two particular angle: one is the angle with minimum azimuthal modulation, the other is the angle with maximum azimuthal modulation and measure their peak amplitude dependence with pump fluence. In Fig 5-10, we could realize there are different slope between this two angles. The angle with maximum azimuthal modulation has a bigger slope, and we propose this phenomenon is caused by the nonlinear effect. In Fig 5-11 and Fig 5-12, the symmetry between “the P-pump P-THz and P-pump S-THz” and “S-pump P-THz and S-pump S-THz” has been shown.



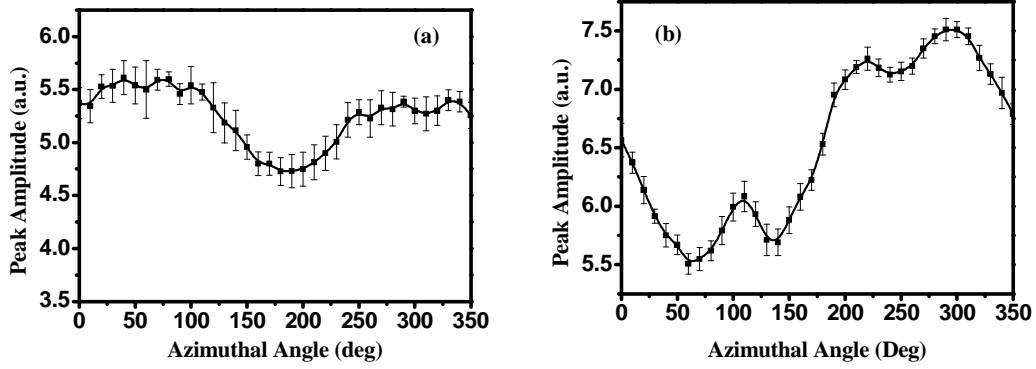


Fig 5-8. Peak amplitude of the p-terahertz fields as function of azimuthal angel rotation of (a) c-plane InN film and (b) a-plane InN excited at 20mW.

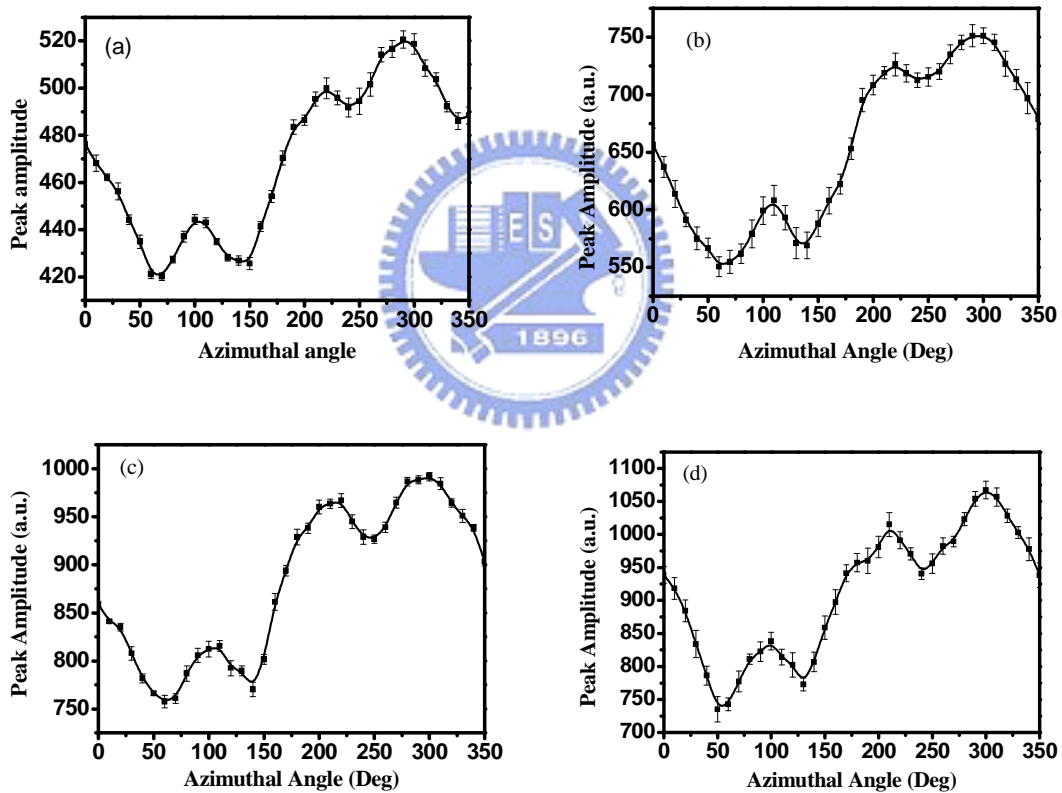


Fig 5-9. Peak amplitude of the p-polarized terahertz fields as function of azimuthal angle rotation of a-plane InN film excited at different fluence (a) 20mW (b) 50mW (c) 75mW (d) 100 mW by p-polarized pump beam.

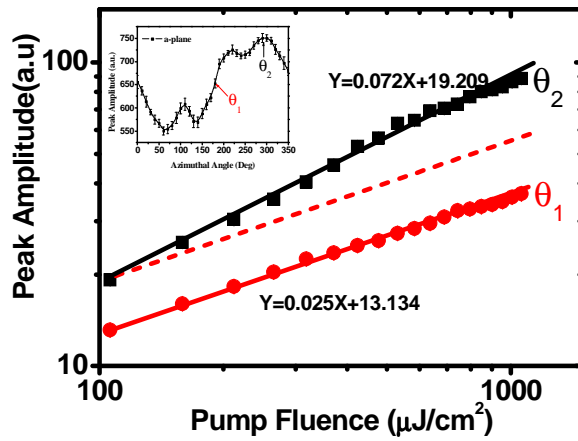


Fig 5-10 The amplitude of the p-polarized THz emission field vs pump fluence at the different azimuthal angle. θ_1 is the angle with minimum azimuthal modulation and θ_2 is the angle with maximum azimuthal modulation .

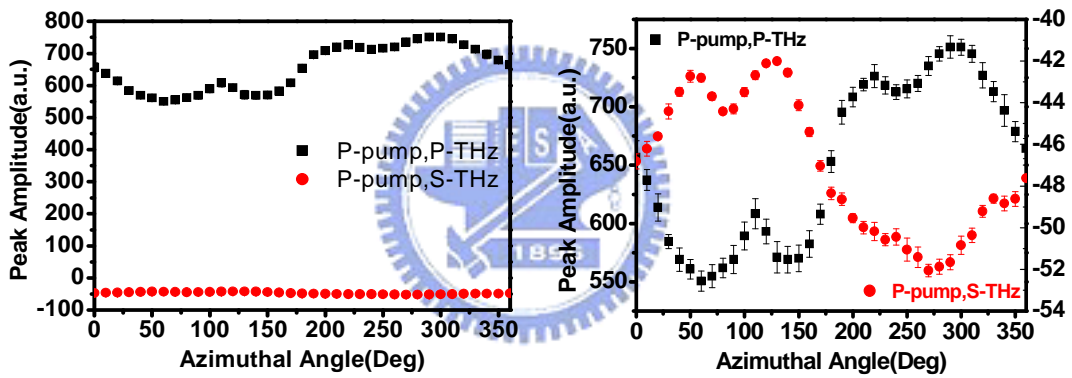


Fig 5-11. Azimuthal-angle dependence of the a-plane InN film with the pump power 50mW and p-polarized pump beam.

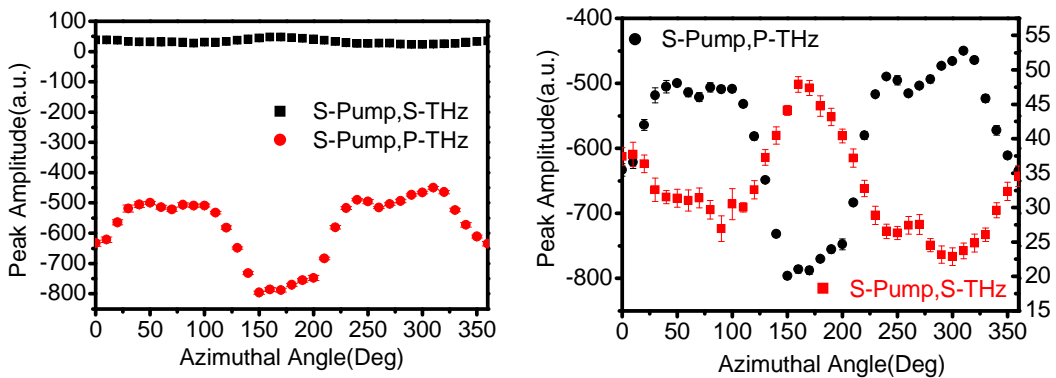


Fig 5-12. Azimuthal-angle dependence of the a-plane InN film with the pump power

50mW and s-polarized pump beam.

5-3 Pump Polarization Dependence of Semiconductors

The pump polarization dependence of thin c-plane InN film was shown[35] :

$$d_{eff}^2 = (d_x \cos \theta_t + d_z \sin \theta_t)^2 + d_y^2 \quad (5-3.1)$$

$$\begin{aligned} d_x &= 2d_{31} \cos^2 \varphi \cos \theta_t \sin^2 \theta_t \\ d_y &= 2d_{31} \cos \varphi \sin \varphi \sin^2 \theta_t \\ d_z &= d_{31} \cos^2 \varphi \cos^2 \theta_t + d_{31} \sin^2 \varphi + d_{33} \cos^2 \varphi \sin^2 \theta_t \end{aligned} \quad (5-3.2)$$

θ_t is the incident angle for the pump beam inside the film, and the x and y axis are chosen to be parallel to and perpendicular to the plane of incidence, respectively. By assuming that $d_{31} = d_{15}$ and $d_{33} = -2d_{15}$ and the incident angle $\theta_i = 60^\circ$, d_{eff}^2 becomes to :

$$\begin{aligned} d_{eff}^2 &= d_{15}^2 A_1^2 \left\{ (5A_1 - 4) [5A_1 \cos^4 \varphi - 2 \cos^2 \varphi] + 1 \right\} \\ A_1 &= \sin \theta_t = \frac{\sin 60^\circ}{n_{InN}} = \frac{\sqrt{3}}{2n_{InN}} \end{aligned} \quad (5-3.3)$$

and d_{eff}^2 is plotted versus φ . The pump-polarization dependence of p-polarized terahertz peak amplitude generated from c-plane InN is shown on Fig 5-13. From that, we could see that when the pump beam is p-polarized (i.e. 0° , 180° and 360°), the THz power reaches the maximum values. On the other hand, when the polarization angles for the pump beam measured with respect to the p-polarization direction are within the range 60° - 120° , the output powers are quite low.

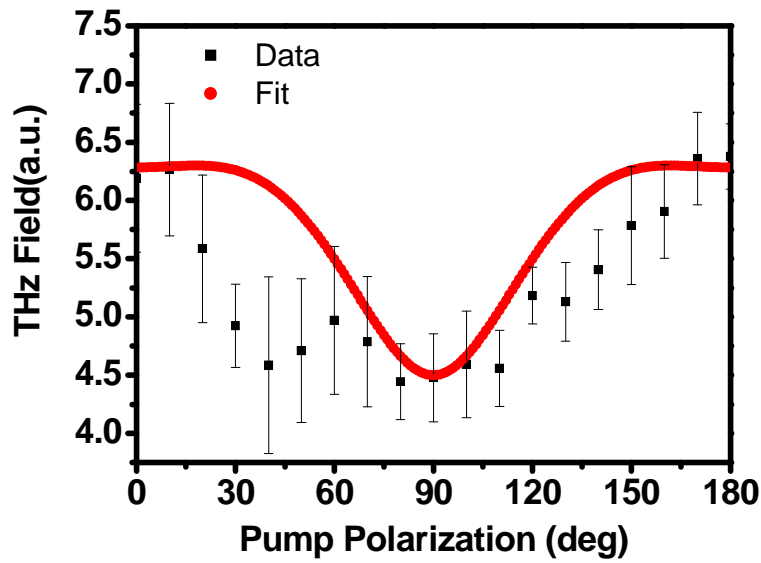


Fig 5-13. Pump polarization angle dependence of THz peak amplitude of c-plane InN. The pump polarization is p-polarization when angles are at 0° , 180° , 360° and s-polarization when angles are at 90° , 270° . The maximum peak is at the p-pump and the minimum peak amplitude at the s-pump.

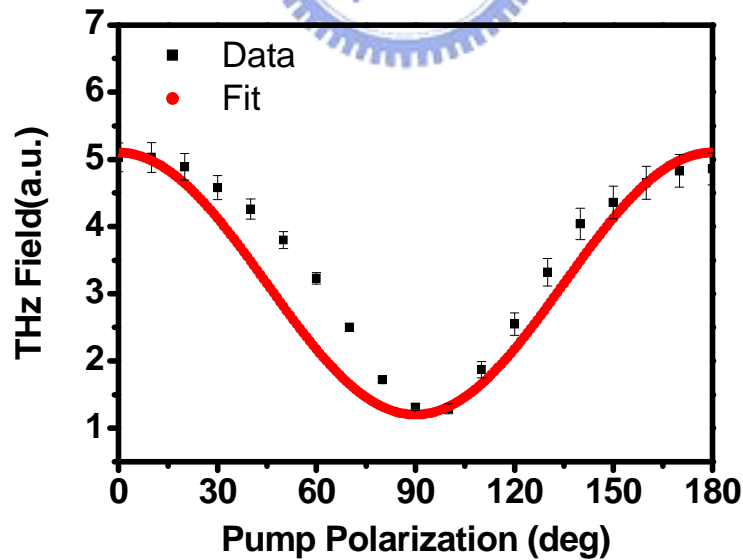


Fig 5-14 Pump polarization angle dependence of THz peak amplitude of n-type InAs.

The dependence of n-type InAs is the same as c-plane InN and shown on Fig 5-14.

However, in the Fig 5-155, it shows that peak amplitude of the p-polarized terahertz fields as function of pump polarization of a-plane InN. There is a quite different phenomenon from c-plane InN film. The p-polarized and s-polarized pump beam generate almost equal amount of terahertz amplitude but opposite polarity from a-plane InN film. However, up to now, we haven't known the susceptibility tensor χ of a-plane InN, and we couldn't make a theoretical model to fit this experiment curve. But in the paper published by J.E. Sipe et al.[43], they showed that the electric field radiation from the surface contribution of (100) cubic centro-symmetric crystals is bound up with the polarization of incident laser beam:

$$\vec{E}_p \propto C_1 E_{i(s)}^2 + C_2 E_{i(p)}^2, \quad \vec{E}_s \propto E_{i(s)} E_{i(p)} \quad (5-3.3)$$

C_1 , C_2 , and C_3 are the coefficients about the susceptibility tensor. If the THz radiation of the a-plane InN is proportional to $\mathbf{E}_s \cdot \mathbf{E}_p$, we could use the mathematic operation : $E_s = E \cos\theta$, $E_p = E \sin\theta$, $E_{THz} \propto E_s * E_p = E \sin 2\theta$. That is, the p-polarized and s-polarized pump beam both generate almost equal amount of terahertz amplitude but opposite polarity. But this is just a conjecture, in order to realize the mechanism of pump polarization dependence, so we also need to know the detailed structure of a-plane InN film.

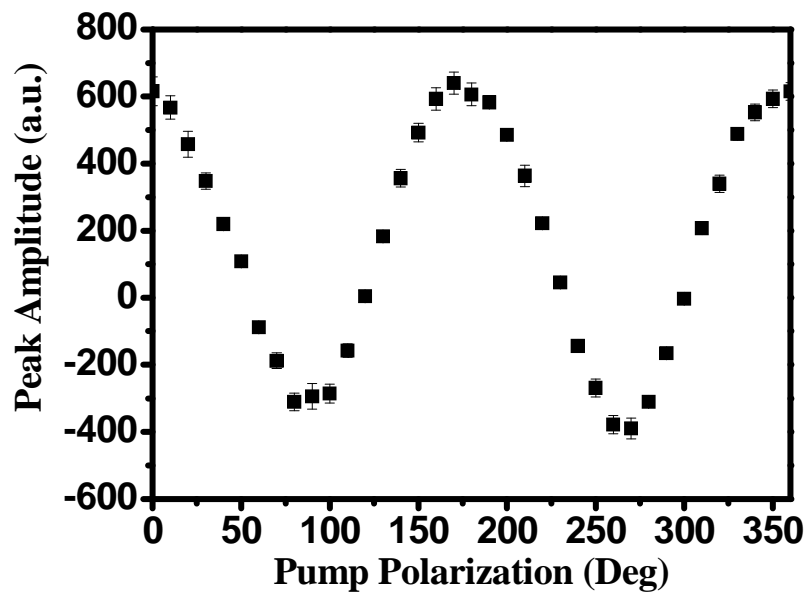


Fig 5-15. Peak amplitude of the p-polarized terahertz fields as function of pump polarization of a-plane InN excited at 20mW. The pump polarization is p-polarization when angles are at 0° , 180° , 360° and s-polarization when angles are at 90° , 270° .



Chapter 6 Conclusion and Future Work

6-1 Conclusion

In this thesis, we have investigated a significant enhancement in terahertz emission from the indium nitride (InN) films grown along the a-axis. The a-plane InN film could enhance two orders of the power of THz emission, and the acceleration of photoexcited carriers along in-plane electric field might be responsible for this drastic power enhancement

Thus, THz emission from the a-plane InN film would have the same orders as that from n-type InAs. Otherwise, we also measured the azimuthal angle dependence of a-plane InN film which shows that the p-polarized terahertz output combines with two contribution: a large angularly independent component (due to the accelerated photo-carriers in the in-plane electric field of the a-plane InN film) and a weak angularly dependent component (due to nonlinear optical process). In the measurement of pump polarization dependence of the peak THz emission amplitude, there is a quite different phenomenon from c-plane InN film. The p-polarized and s-polarized pump beam generate almost equal amount of terahertz amplitude but opposite polarity from a-plane InN film.

6-2 Future Work

We need to know more information about the band structure and the susceptibility tensor χ of a-plane InN film so that we could use theoretical simulation to explain the phenomenon of the azimuthal-angle dependence and pump-polarization dependence of peak amplitude.



Reference

- [1] Mourou G, Stancampiano C V, Antonetti A and Orszag A, "Picosecond microwave pulse generation," *Appl. Phys. Lett.*, **38**, no. 6, pp. 470-472, 1981.
- [2] Auston D H, Cheung K P and Smith P R, "Picosecond photoconducting Hertzian dipoles," *Appl. Phys. Lett.*, **45**, no. 3, pp. 284-286, 1984.
- [3] Ch. Fattinger, and D. Grischkowsky, "Point source terahertz optics," *Appl. Phys. Lett.*, **53**, pp. 1480-1482, 1988.
- [4] N. Sarukura, H. Ohtake, S. Izumida, and Z. Liu, "High average-power THz radiation from femtosecond laser-irradiated InAs in a magnetic field and its elliptical polarization characteristics," *J. Appl. Phys.*, **84**, pp. 654-656, 1998.
- [5] X.-C. Zhang, *Perspectives in Optoelectronics*, Ed. By Sudhanshu S. Jha, World Scientific, chapter 3, 1995.
- [6] Q. Wu and X. C. Zhang, "Ultrafast electro-optic field sensors," *Appl. Phys. Lett.*, **68**, no. 12, pp. 1604-1606, 1996.
- [7] A. G. Markelz, A. Roitberg, and E. J. Heilweil, "Pulsed terahertz spectroscopy of DNA, bovine serum albumin and collagen between 0.1 and 2.0 THz," *Chem. Phys. Lett.* **320**, pp. 42-48, 2000.
- [8] B.B. Hu and M. C. Nuss, "Imaging with terahertz waves," *Opt. Lett.*, **20**, pp. 1716-1718, 1995
- [9] D. Grischkowsky, S. Keiding, M. van Exter, and Ch. Fattiger, "Far-infrared Time-domain Spectroscopy with Terahertz Beams of Dielectrics and Semiconductors," *J. Opt. Soc. Am. B*, **7**, No. 10, pp. 2006-2015, 1990.
- [10] M. van Exter and D. Grischkowsky, "Optical and Electronic Properties of Doped Silicon From 0.1 to 2 THz," *Appl. Phys. Lett.*, **56**, no. 17, pp. 1694-1696 1990.

- [11] Matthew C. Beard, Gordon M. Turner, James E. Murphy, Olga I. Micic, Mark C. Hanna, Arthur J. Nozik, and Charles A. Schmuttenmaer, "Electronic Coupling in InP Nanoparticle Arrays" *Nano Lett.*, **3**, pp. 1695-1699
- [12] Jason B. Baxter and Charles A. Schmuttenmaer, "Conductivity of ZnO Nanowires, Nanoparticles, and Thin Films Using Time-Resolved Terahertz Spectroscopy," *J. Phys. Chem. B*, **110**, pp.25229-25239, 2006
- [13] D. G. Cooke, A. N. MacDonald,¹ A. Hryciw, J. Wang, Q. Li, A. Meldrum, and F. A. Hegmann, "Transient terahertz conductivity in photoexcited silicon nanocrystal films," *Phys. Rev. B*, **73**, pp. 193311-1-193311-4, 2006
- [14] R. Acsazubi, I. Wilke, K. Denniston, H. L. Lu, and W. J. Schaff, "Terahertz emission by InN," *Appl. Phys. Lett.*, **84**, pp. 4810-4812, 2004.
- [15] G. D. Chern, E. D. Readinger, H. Shen, M. Wraback, C. S. Gallinat, G. Koblmuller, and J. S. Speck, "Excitation wavelength dependence of terahertz emission from InN and InAs," *Appl. Phys. Lett.*, **89**, pp.141115, 2006.
- [16] B. Pradarutti, G. Matthaus, C. Bruckner, S. Riehemann, G. Notni, S. Nolti, V. Cimalla, V. Lebedev, O. Ambacher, and A. Tunnermann, "InN as THz Emitter excited at 1060 nm and 800 nm," *Proc. of SPIE*, **6194**, pp.619401, 2006.
- [17] P.K. Benicewicz, J.P. Roberts, and A.J. Taylor, "Scaling of terahertz radiation from large-aperture boomed photoconductors," *J. OPT. Soc. Am. B*, **11**, pp.2533-2545, 1994.
- [18] X.-C. Zhang and D.H. Auston, "Optoelectronic measurement of semiconductor surface and interface with femtosecond optics," *J. Appl. Phys.*, **71**, pp.326-338, 1991
- [19] W. Monch, "Semiconductor Surface and Interface," Springer, Berlin, Heidelberg pp. 68, 1993

- [20] V. M. Polyakov and F. Schwierz, “Low-field electron mobility in wurtzite InN”, Appl. Phys. Lett. **88**, 032101, 2006
- [21] M Levinshtein, S Rumyantsev (*Ioffe Institute*) & M Shur, “Handbook Series on Semiconductor Parameters Vol. 1”, World Scientific Publishing Company, 1996
- [22] S. Chuang, S. Schmitt-Rink, B. Greene, P. Saeta, A. Levi, ” Optical rectification at semiconductor surfaces”, Phys. Rev. Lett. **68**, 102, 1995
- [23] A. Bonvalet, M. Joffre, J. Martin, A. Migus, ” Generation of ultrabroadband femtosecond pulses in the mid-infrared by optical rectification of 15 fs light pulses at 100 MHz repetition rate”, Appl. Phys. Lett. **67**, 2907,1995
- [24] A. Rice, Y. Jin, X.Ma, X.-C. Zhang, D. Bliss, J. Larkin, M. Alexander, “Terahertz optical rectification from <110> zinc-blende crystals”, Appl. Phys. Lett. **64**, 1324, 1994
- [25] P. Gu, M. Tani, S. Kono, K. Sakai, ” Study of terahertz radiation from InAs and InSb”, J. Appl. Phys. **91**, 5533 , 2002
- [26] D. Mittleman, “Sensing with Terahertz Radiation,” Springer, Berlin, Heidelberg pp.155, 2002
- [27] H. Ahn, Y.-P. Ku, Y.-C. Wang, C.-H. Chuang, “Terahertz emission from vertically aligned InN nanorod arrays”, Appl. Phys. Lett. **91**, 132108 , 2007
- [28] X. C. Zhang, Y. Liu, T. D. Hewitt, T. Sangsiri, L. E. Kingsley, and M.Weiner, “Magnetic switching of THz beams” Appl. Phys. Lett. **62**, 2003 (1993).
- [29] S. C. Howells, S. D. Herrera, and L. A. Schlie, “” Infrared wavelength and temperature dependence of optically induced terahertz radiation from InSb”, Appl. Phys. Lett. **65**, 2946(1994).)

- [30] M. B. Johnston, D. M. Whittaker, A. Corchia, A. G. Davies, and E. H. Linfield, "Simulation of terahertz generation at semiconductor surfaces", *Phys. Rev. B* , **65**, 165301 , 2002
- [31] Elmer Estacio, Hisashi Sumikura, Hidetoshi Murakami, Masahiko Tani, Nobuhiko Sarukura, and Masanori Hangyo, Carlito Ponceca, Jr., Romeric Pobre, and Reuben Quiroga, Shingo Ono, "Magnetic-field-induced fourfold azimuthal angle dependence in the terahertz radiation power of (100) InAs", *Appl. Phys. Lett.*, **90**, 151915 , 2007
- [32] B. Pradarutti, G. Matthäus, C. Brückner, S. Riehemann, G. Notni, S. Nolti, V. Cimalla, V. Lebedev, O. Ambacher, and A. Tünnermann, "InN as THz emitter excited at 1060 and 800 nm", *Proc. SPIE* **6194**, 619401, 2006.
- [33] Xiaodong Mu, Yujie J. Ding, Kejia Wang, Debdeep Jena, and Yuliya B. Zotova, "Resonant terahertz generation from InN thin films", *OPTICS LETTERS* **32**, No. 11, June 1, 2007
- [34] M. Reid and R. Fedosejevs, "Terahertz emission from (100) InAs surfaces at high excitation fluences", *Appl. Phys. Lett.*, **86**, 011906 2005
- [35] Xiaodong Mu, Yujie J. Ding, Kejia Wang, Debdeep Jena, and Yuliya B. Zotova , " Resonant terahertz generation from InN thin films", *Optics Letters*, Vol.**32** No.11, 2007
- [36] V. Yu. Davydov, A. A. Klochikhin, R. P. Seisyan, V. V. Emtsev, S. V. Ivanov, F. Bechstedt, J. Furthmüller, H. Harima, A. V. Mudryi, J. Aderhold, O. Semchinova, and J. Graul, "Absorption and Emission of Hexagonal InN. Evidence of Narrow Fundamental Band Gap", *Phys. Status Solidi B* ,**229**, R1 (2002)

- [37] V. Yu. Davydov, A. A. Klochikhin, V. V. Emtsev, D. A. Kurdyukov, S. V. Ivanov, V. A. Vekshin, F. Bechstedt, J. Furthmüller, J. Aderhold, J. Graul, A. V. Mudryi, H. Harima, A. Hashimoto, A. Yamamoto, and E. E. Haller, "Band Gap of Hexagonal InN and InGaN Alloys", *Phys. Status Solidi B*, **234**, 787 (2002)
- [38] J. Wu, W. Walukiewicz, K. M. Yu, J. W. Ager II, E. E. Haller, H. Lu, W. J. Schaff, Y. Saito, and Y. Nanishi, "Unusual properties of the fundamental band gap of InN" *Appl. Phys. Lett.* **80**, 3967 (2002)
- [39] J. Wu, W. Walukiewicz, W. Shan, K. M. Yu, J. W. Ager III, S. X. Li, E. E. Haller, H. Lu, and W. J. Schaff, J. "Temperature dependence of the fundamental band gap of InN" *Appl. Phys.* **94**, 4457 (2003)
- [40] K. Xu and A. Yoshikawa, "Effects of film polarities on InN growth by molecular-beam epitaxy" *Appl. Phys. Lett.* **83**, 251 (2003)
- [41] T. Matsuoka, H. Okamoto, M. Nakao, H. Harima, and E. Kurimoto, "Optical bandgap energy of wurtzite InN", *Appl. Phys. Lett.* **81**, 1246 (2002).
- [42] Hai Lu, William J. Schaff, and Lester F. Eastman, "Growth of *a*-plane InN on *r*-plane sapphire with a GaN buffer by molecular-beam epitaxy", *Appl. Phys. Lett.* **83**, 1136 (2003)
- [43] J. E. Sipe, D.J. Moss, and H. M. van Driel, "Phenomenological theory of optical second- and third-harmonic generation from cubic centrosymmetric crystals", *Phys. Rev. B*, **35**, 1129, (1987)
- [44] C. Weiss, R. Wallenstein, and R. Beigang, "Magnetic-field-enhanced generation of terahertz radiation in semiconductor surfaces", *Appl. Phys. Lett.* **77**, 4160 (2000).

- [45] N. Sarukura, H. Ohtake, S. Izumida, and Z. Liu, “High average-power THz radiation from femtosecond laser-irradiated InAs in a magnetic field and its elliptical polarization characteristics”, J. Appl. Phys. **84**, 654 (1998)
- [46] R. McLaughlin, A. Corchia, M. B. Johnston, Q. Chen, C. M.Ciesla, D. D. Arnone, G. A. C. Jones, E. H. Linfield, A. G.Davies, and M. Pepper, “Enhanced coherent terahertz emission from indium arsenide in the presence of a magnetic field”, Appl. Phys. Lett. **76**, 2038 (2000)
- [47] D. Segev and C. G. van de Walle, “Electronic structure of nitride surfaces”, J. Crystal Growth **300**, 199 (2007)

